Patterns of bacterial motility in microfluidics-confining environments

Viola Tokárová[a,b,1], Ayyappasamy Sudalaiyadum Perumal[a,1], Monalisha Nayak[a,1], Henry Shum[c,1], Ondřej Kašpar[a,b], Kavya Rajendran[a], Mahmood Mohammadi[d], Charles Tremblay[d], Eamonn A. Gaffney[e], Sylvain Martel[d], Dan V. Nicolau Jr[e], and Dan V. Nicolau[a,2]

[a]Faculty of Engineering, Department of Bioengineering, McGill University, Montreal, QC H3A 0C3, Canada; [b]Department of Chemical Engineering, University of Chemistry and Technology, Prague, 166 28 Prague, Czech Republic; [c]Department of Applied Mathematics, University of Waterloo, Waterloo, ON N2L 3G1, Canada; [d]Department of Computer Engineering, École Polytechnique de Montréal, Montreal, QC H3T 1J4, Canada; and [e]School of Mathematical Sciences, Queensland University of Technology, Brisbane, QLD 4000 Australia

Edited by Robert H. Austin, Princeton University, Princeton, NJ, and approved March 19, 2021 (received for review July 5, 2020)

Understanding the motility behavior of bacteria in confining microenvironments, in which they search for available physical space and move in response to stimuli, is important for environmental, food industry, and biomedical applications. We studied the motility of five bacterial species with various sizes and flagellar architectures (*Vibrio natriegens*, *Magnetococcus marinus*, *Pseudomonas putida*, *Vibrio fischeri*, and *Escherichia coli*) in microfluidic environments presenting various levels of confinement and geometrical complexity, in the absence of external flow and concentration gradients. When the confinement is moderate, such as in quasi-open spaces with only one limiting wall, and in wide channels, the motility behavior of bacteria with complex flagellar architectures approximately follows the hydrodynamics-based predictions developed for simple monotrichous bacteria. Specifically, *V. natriegens* and *V. fischeri* moved parallel to the wall and *P. putida* and *E. coli* presented a stable movement parallel to the wall but with incidental wall escape events, while *M. marinus* exhibited frequent flipping between wall accumulator and wall escaper regimes. Conversely, in tighter confining environments, the motility is governed by the steric interactions between bacteria and the surrounding walls. In mesoscale regions, where the impacts of hydrodynamics and steric interactions overlap, these mechanisms can either push bacteria in the same directions in linear channels, leading to smooth bacterial movement, or they could be oppositional (e.g., in mesoscale-sized meandered channels), leading to chaotic movement and subsequent bacterial trapping. The study provides a methodological template for the design of microfluidic devices for single-cell genomic screening, bacterial entrapment for diagnostics, or biocomputation.

bacterial motility | microfluidic devices | space partitioning | wall escaper | wall accumulator

Many motile bacteria live in confining microenvironments (e.g., animal or plant tissue, soil, waste, granulated, and porous materials) and consequently are important to many applications like health [infectious diseases (1, 2), pharmaceuticals (3), and nutrition (4)], agriculture [veterinary (5) and crops (6)], environmental science [photosynthesis (7), biodegradation (8), and bioremediation (9)], and industrial activities [mining (10) and biofouling (11)]. Bacterial motility is essential in the search for available physical space as well as for enabling bacterial taxis in response to external stimuli, such as temperature (12), chemical gradients (13, 14), mechanical cues (15), or magnetic fields (16).

To thrive in environments with diverse geometrical and physical characteristics, from open spaces to constraining environments, motile bacteria have evolved a multitude of propelling mechanisms (17), with flagellum-driven being the most common (18, 19). Flagellum-based machinery features various numbers of flagella (20) and designs: monotrichous, lophotrichous, amphitrichous, or peritrichous. The mechanics of this machinery, coupled with cell morphology (21) (e.g., coccus, rod-like, or curved) translates into several motility modes (e.g., turn angle, run-and-tumble, or run-and-flick) (22), and various motility behaviors (e.g., swimming, tumbling, and swarming) (17, 23). Environmental factors (24, 25) (e.g., chemical composition, viscosity, temperature, pH, and the chemistry and the roughness of adjacent surfaces) also influence bacterial motility.

"Pure" bacterial motility, unbiased by chemotaxis or fluid flow, was reported near simple flat surfaces (26, 27) and in channels (28–30). Simulations of model bacteria in analogous conditions were also undertaken (31–37), but owing to the complexity of bacterial mechanics (38), modeling from first principles did not provide sufficient understanding to accurately predict movement patterns of different species in complex, confined environments. Consequently, studies of the effects of bacterial geometry in confined geometries were limited to models of simple, monotrichous bacteria with an assumed rigid flagellum (32, 39).

Microfluidic devices (40, 41) are commonly used for the manipulation of individual or small populations of cells in micrometer-sized channels for medical diagnostics (42), drug screening (43), cell separation (44, 45), detection and sorting (46), and single-cell genomics (47). While microfluidic structures are used for the study of

Significance

Understanding bacterial movement is crucial for health, agriculture, environment, and industry. Studying the motility of five bacterial species in microfluidic environments showed that bacterial motility behavior is the result of a "tug-of-war" between hydrodynamics and local nanomechanics. In less confining spaces, bacterial motility is governed by hydrodynamics and can be approximately predicted by modeling developed for the simplest species. Conversely, in tightly confining environments, movement is mainly controlled by the steric interactions between flagella and the surrounding walls. Intriguingly, in mesoscale-sized geometries, hydrodynamics and bacterium–wall interactions overlap, either "constructively," leading to smooth movement in straight channels, or "destructively," leading to trapping. Our study provides a methodological template for the development of devices for single-cell genomics, diagnostics, or biocomputation.

Author contributions: D.V.N. designed research; V.T., A.S.P., M.N., H.S., O.K., M.M., C.T., and D.V.N. Jr. performed research; S.M. contributed new reagents/analytic tools; V.T., A.S.P., M.N., H.S., O.K., K.R., E.A.G., D.V.N. Jr., and D.V.N. analyzed data; and V.T., A.S.P., M.N., H.S., O.K., and D.V.N. wrote the paper.

The authors declare no competing interest.

This article is a PNAS Direct Submission.

[1]V.T., A.S.P., M.N., and H.S. contributed equally to this work.

[2]To whom correspondence may be addressed. Email: dan.nicolau@mcgill.ca.

This article contains supporting information online at https://www.pnas.org/lookup/suppl/doi:10.1073/pnas.2013925118/-/DCSupplemental.

Published April 19, 2021.

the motility of mammalian cells (48, 49), and microorganisms [e.g., fungi (50, 51), algae (52), or bacteria (29, 53–56)], these studies typically focus on a single species.

To make progress toward a more general understanding of the motility of individual bacterial cells in confining microenvironments, as well as to assess the extent to which the behavior of bacteria with complex architectures can be assimilated with that of the more predictable monotrichous bacteria, the present work investigated the movement of five species (i.e., *Vibrio natriegens*, *Magnetococcus marinus*, *Pseudomonas putida, Vibrio fischeri*, and *Escherichia coli*) in microfluidic geometries with various levels of confinement and geometrical complexity.

Results and Discussion

The modulation of motility behavior by confinement was assessed by observing, by three-dimensional (3D) imaging, the movement of individual bacteria, presenting various characteristics (Fig. 1*A* and *SI Appendix*, Fig. S1) in microfluidic structures with high (6 μm) or low (4 μm) ceilings (Fig. 1*B*) and with various geometries (Fig. 1*C* and *SI Appendix*, Fig. S2) as follows: 1) large chambers with quasi-open spaces ("plazas"), 2) linear channels with various widths, 3) channels presenting lateral exits at various angles, and 4) meandered channels with various widths. In the absence of pressure and concentration gradients, this approach allowed the study of the interaction between hydrodynamics and the steric interactions of bacteria with the walls, unobscured by other external factors (e.g., rheo- and chemotaxis). Experimental, image analysis, and simulation protocols are fully described in *SI Appendix*.

Motility in Large Chambers.

Impact of the distance between horizontal planes. To minimize the possible coupling of the impact of horizontal planes, the designs of microfluidic chambers, made of polydimethylsiloxane (PDMS), had to find a compromise between their height and fabrication and operation issues. From the design perspective, it was found that a height of 6 μm (Fig. 1*A* and *SI Appendix*, Table S1) allows, conservatively, the unencumbered bacterial motility. Furthermore, preliminary experiments comparing motility in both types of microfluidic structures presented evidence (Movie S1) of the coupling of the impact on both horizontal planes on bacterial motility for those with 4 μm heights. Consequently, 6 μm–tall microfluidic structures were used for all further experiments. A detailed discussion is presented in *SI Appendix*.

Spatial distribution of bacteria. The bacterial species studied presented different motility behaviors with respect to proximity of vertical walls and corners (Fig. 2 *A*–*C*). First, *V. fischeri*, *V. natriegens*, and *E. coli* moved at small distances from vertical walls. Second, *M. marinus* presented an uneven, broken density near vertical walls, due to the frequent "ping-pong"–like collisions and reflections (Movie S1). Third, *P. putida* presented an even spatial distribution throughout the chamber.

The 3D imaging and z-stack sectioning of bacterial trajectories in 6 μm–tall plazas (Fig. 2*D* and *SI Appendix*, Figs. S6–S8) revealed a similar behavior in the central area close to the horizonal walls (i.e., free of the possible edge effects from the vertical walls). *V. natriegens*, *V. fischeri*, and *E. coli* presented trajectories in proximity to—and parallel with—the horizontal walls. This was not the case

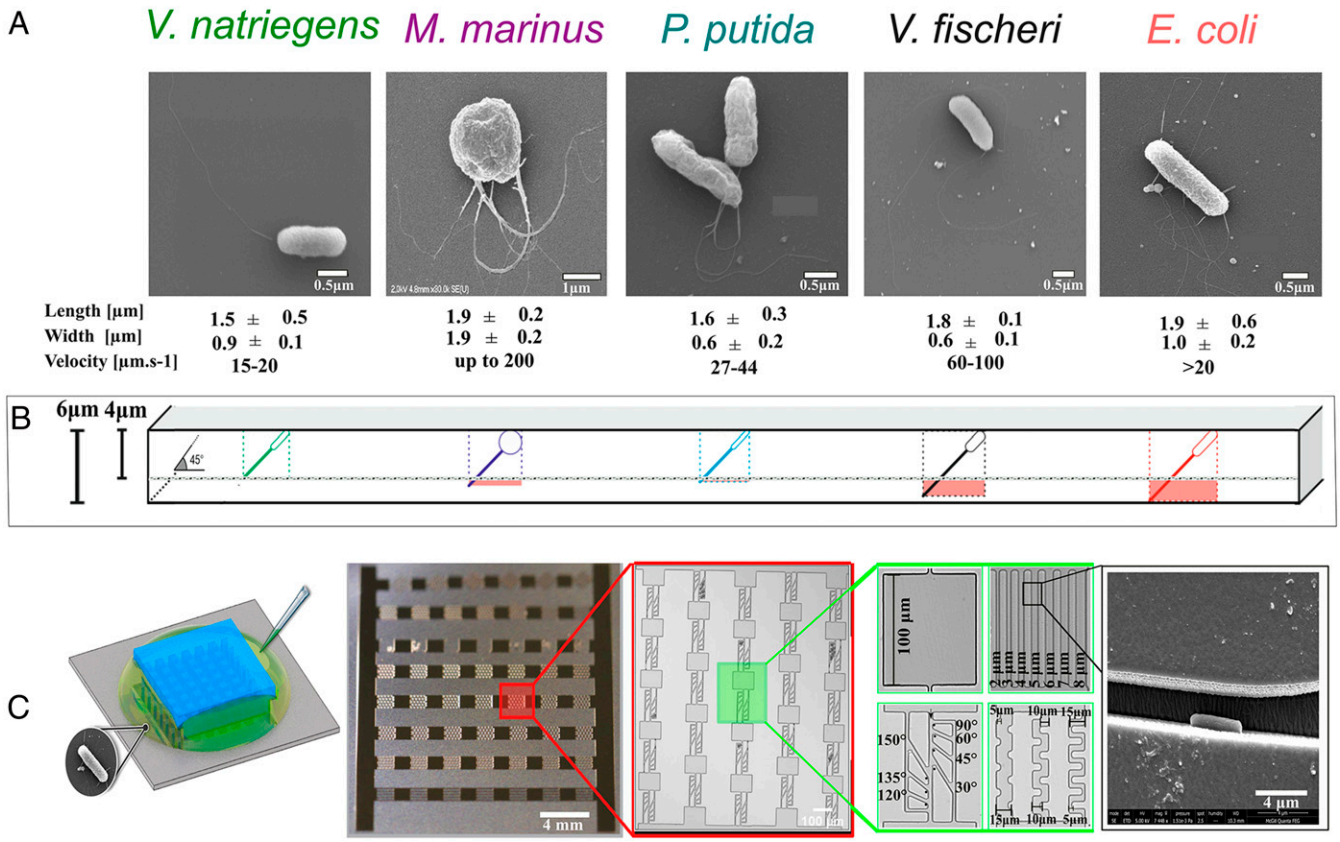

Fig. 1. Microfluidics chip for testing microbial motility. (*A*) Scanning electon micrographs (SEM) images of bacteria studied with various architectures and dimensions (full details in *SI Appendix*, Table S1). (*B*) Graphical projection of the fit of the total bacterial length (body plus flagella) positioned at 45° versus the height of the microfluidic structures for 6 μm and 4 μm heights. (*C*) Sequential, from left to right, zoom-in images of the experimental device: 1) the bacterial suspension is introduced from the side of the chip attached to the cover slide; 2) the overall architecture of the chip; 3) zoom-in of one lane of experimental structures (sequence of angled channels separated by plazas); 4) detailed image of the experimental structures used in this study (i.e., plazas) and linear channels (top row), angled, and meandered channels (bottom row); and 5) SEM image of a bacterium (here, *E. coli*) in a channel.

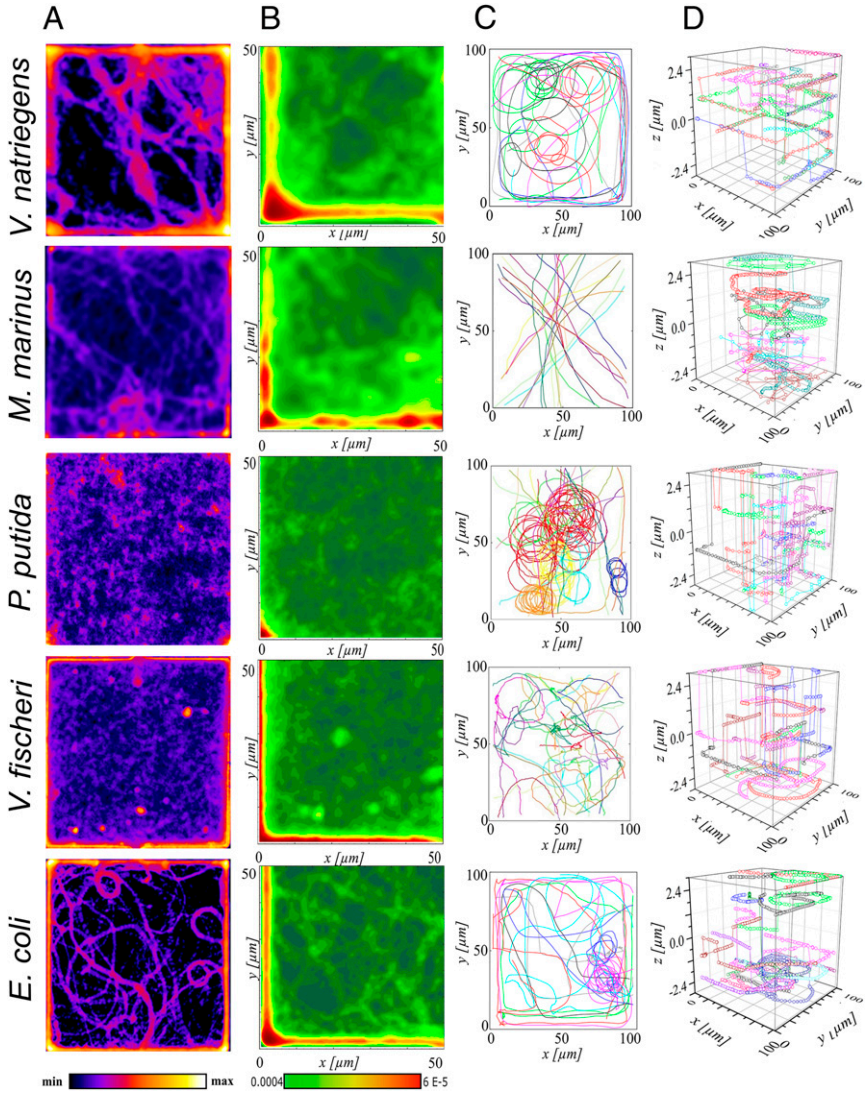

Fig. 2. Motility in plazas with 6 μm high ceilings. (*A*) Density maps of bacterial locations. Color code (bottom): "min" and "max" represent no and the highest presence of bacteria, respectively. (*B*) Spatial distribution of bacteria obtained by superimposing and averaging the data from all four quarters of the density maps in *A*. Color code (bottom): frequency of bacterial presence, with red for the highest and dark green for the minimum probability. (*C*) Characteristic long2D projections of bacterial trajectories. (*D*) 3D bacterial trajectories. By rows, from top to bottom, are the following: *V. natriegens* (average count of bacterial positions in each frame, n = 14/frame); *M. marinus* (n = 12/frame); *P. putida* (n = 15/frame); *V. fischeri* (n = 15/frame); and *E. coli* (n = 13/frame). Movie S1 presents the bacterial movement in plazas, with representative trajectories (similar to *C*).

for *P. putida* and *M. marinus*, which frequently fluctuated between z-planes (*SI Appendix*, Figs. S7 and S8). Statistical analysis of the bacterial positions (*SI Appendix*, Fig. S9) showed that *V. natriegens*, *V. fischeri*, and *E. coli* moved preferentially in a parallel plane to the horizontal walls and that *P. putida* and *M. marinus* presented a rather uniform distribution of positions on the vertical axis.

Theoretical classification of bacterial motility behavior. For bacteria that are propelled by a flagellum or flagellar bundle behind the cell, the fluid flow generated by swimming has a dipolar structure: the fluid is pushed backward by the flagellum and pulled forward by the cell body. This flow has been shown to attract swimmers to solid walls, causing them to remain close to the wall for long time periods despite rotational Brownian motion (57). A separate effect of swimming near surfaces is that hydrodynamic interactions between the wall and rotating flagellum and between the wall and counter-rotating cell body, respectively, lead to bacteria swimming in circular orbits when they are close to a wall (58).

Detailed hydrodynamic modeling of monotrichous bacteria showed that the geometrical parameters of the cell (length and width) and of the helical flagellum (length, helical amplitude, and wavelength) determine the motility behavior near a single flat surface (32). Based on this modeling framework, correlated with the experimental observations from the present study, three classes of behavior were observed, depending on the geometry of the bacterium. "Wall accumulators" descend to the walls and exhibit a strong propensity for swimming in the closest vicinity to the wall (with a separation of tens of nanometers between the bacterium and the surface), where steric interactions are likely, thus making difficult the precise prediction of motility behavior even for the simplest monotrichous bacteria. When bacteria swim at distances further than this from the wall but at a nearly constant separation, exhibiting the characteristic circular orbits predicted by simpler analysis, they are classified as "stable swimmers parallel to the wall." It was observed (26) that dynamical interactions are negligible before collisions with the walls, but once bacteria swim on parallel planes a few micrometers away from surfaces, hydrodynamic forces

maintain long residence times in this region. Finally, when hydrodynamic interactions result in bacterial movement away from surfaces, they are classified as "wall escapers." The demarcation between these classes is approximate, due to the inherent stochasticity of bacterial motility.

Two key geometrical parameters determining whether a particular bacterium is an accumulator, escaper, or moving parallel to the wall are 1) the cell body aspect ratio and 2) the length of the flagellum. Higher aspect ratios (more rod-like) and shorter flagella encourage escape from walls (Fig. 3). For geometries at the boundary between parallel motion and escapers, it is possible for a bacterium to exhibit either stable motion close to the wall or escape depending on the angle of approach to the wall. It is useful to first determine the behavior of bacteria near a single wall because this is indicative of motility in more complex environments. For example, simulations showed that parallel–stable swimmers and escapers had different characteristics when placed between parallel walls (35) and in corners of rectangular channels (39). However, the variability of characteristic bacterial dimensions adds to the inherent stochasticity of movement. This in turn makes the demarcation between motility classes approximate. Details of the modeling used in Fig. 3 are given in *SI Appendix*, and the characteristic dimensions of bacteria are presented in *SI Appendix*, Table S2.

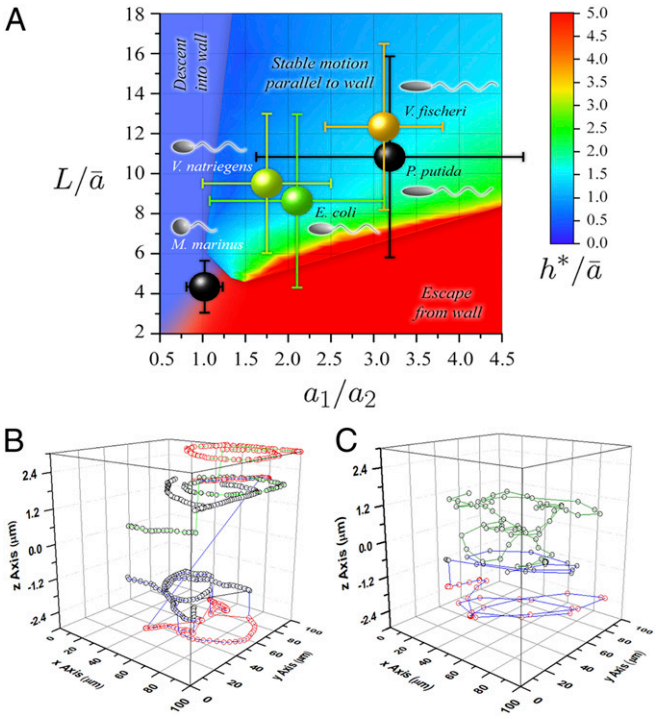

Fig. 3. Prediction of motility behavior. (*A*) Bacterial positions, according to their dimensions, on a motility "map" (32), derived from hydrodynamic principles, for monotrichous bacteria. *V. natriegens*, *V. fischeri*, and *E. coli*, "swim parallel to walls" (confirmed experimentally, Fig. 2*B* and *SI Appendix*, Fig. S9). *M. marinus* is placed at the boundary between "wall accumulators" and "wall escapers" regions (confirmed experimentally by its wall-bouncing behavior). *P. putida*, with the largest variability of sizes, straddles the extreme "swimming parallel to wall" and "wall escaper" regions (confirmed by spatial distribution in Fig. 2*B* and *SI Appendix*, Fig. S9). The legend (updated from ref. 32, *SI Appendix*, Table S2) is as follows: a_1 = polar radius of cell body (half the cell length); a_2 = equatorial radius of cell body (half of the diameter diameter); [a_1/a_2] = aspect ratio of the cell body; L = curvilinear length of the flagellum (approximated by the axial length of the flagellum); $\bar{a}$ = radius of sphere with volume of cell body; $L/\bar{a}$ = nondimensional length of the flagellum/a; h* = optimal distance from wall (for swimmers parallel to walls); and $h^*/\bar{a}$ = nondimensional stable distance from wall. The colors of bacterial coordinates approximately replicate the color equivalent to $h^*/\bar{a}$ (determined from z-stack analysis). (*B*) Example of a bacterium moving stable parallel to the walls: *E. coli* (also exhibiting "escape from wall" jumps). (*C*) Example of a "wall escaper" bacterium: *M. marinus*.

While these theoretical studies were based on a model with a single, polar flagellum, it was demonstrated that such models accurately reproduce the experimentally observed radius of curvature of near-wall tracks for *E. coli*, which swim with several flagella (31). Therefore, it is expected that this classification serves as a useful conceptual background for the characterization of motility behavior in relation to a solid surface, even though most of the species in the current study are architecturally more complex than the monotrichous model (here, *V. natriegens*). Indeed, the propensity to move near surfaces was observed experimentally for several nonmonotrichous bacterial species, for instance (extensively) for *E. coli* (26, 27, 30, 31, 57, 59), but also for *Serratia marcescens* (29) and *Pseudomonas aeruginosa* (60).

Comparison of experimental and theoretically predicted behavior. By comparison with monotrichous model bacteria of equivalent dimensions, *M. marinus* is predicted to be a wall accumulator, but it is actually near the boundary between accumulators and escapers (Fig. 3). All other species are expected to maintain stable motion parallel to and near the walls (Fig. 3), although variability within populations is sufficient for some individuals to be classified as escapers. There are elements that correlate well with the predicted motility behavior of simple bacteria with that of the more complex geometries studied as well as explanations for the deviations from this general "motility landscape" (Fig. 3):

1) Our experiments showed that *M. marinus* did not exhibit stable motion parallel to the wall but rather a "ping-pong"–like movement, with abrupt approaches to the walls alternating with equally abrupt breakouts. Recently, a model of the movement of a polar biflagellate bacterium (61), based on *M. marinus*, showed that such wall escaping (scattering) behavior could occur for certain arrangements of the two flagella. Additionally, it was recently reported that *M. marinus* swims with one flagellar bundle in front of the cell body and one behind (62), a mode of motility that is fundamentally different from the monotrichous model.
2) The density maps, probability maps, long trajectories, represented as two-dimensional (2D) projections and in 3D (Fig. 2 *A–D*, respectively) for *P. putida* and *E. coli*, showed characteristics of both escapers, more apparent for *P. putida*, and movement parallel to the wall, more apparent for *E. coli.* The persistent circular orbits indicate motion close to the horizontal walls, and for *E. coli*, the long trajectories along the vertical walls also highlight boundary accumulation. In contrast, the long, relatively straight trajectories through the middle of the chamber and frequent transitions between z-planes represent wall escaping behaviors. These seemingly contradictory observations are, in fact, consistent with the variability found in the measured cell shapes and flagella lengths. While the average values for both *P. putida* and *E. coli* lie within the movement parallel to the wall regime (Fig. 3), the spread of parameters extends considerably into the wall escaper region.
3) Density and probability maps, as well as 2D projections and 3D bacterial trajectories (Fig. 2 *A–D*, respectively), are consistent with the placement of *V. natriegens* and *V. fischeri* deep in the movement parallel to the walls, according to the theoretical predictions in Fig. 3. Both species showed circular trajectories (more prominent in *V. natriegens*) and high densities around the perimeter of the chamber. Interestingly, *V. natriegens* was often observed swimming parallel to the vertical walls but at distances of around 3.5 μm from the wall (Fig. 2*B*) rather than keeping almost in contact with the wall. This type of parallel motion was found in simulations of boundary accumulators in corners of channels (39).

Motility patterns. The longest trajectories of bacterial motility in plazas had characteristics that were the most species specific (Fig. 2*C* and Movie S1, top row). *V. natriegens*, *E. coli*, and *V. fischeri* presented, to various degrees, two classes of trajectories: 1) movement along the vertical and horizontal walls and, when detached, 2) circular motions, until again attaching to the walls. *M. marinus* exhibited a "ping-pong"–like motility pattern, generally following relatively straight paths until it approached and scattered off a vertical wall, resulting in a statistically higher density localized near the walls (due to frequent collisions). There was little discernible movement along the vertical or horizontal walls of the plaza, and no complete circular orbits were observed. Two classes of behavior were present in the longest trajectories of *P. putida*. Some were relatively straight, spanning from one side of the chamber to the other, whereas other trajectories were circular and persisted for many overlapping cycles. Long trajectories around the perimeter of the chamber, as observed for *V. natriegens*, *E. coli*, and even *V. fischeri*, were uncommon for *P. putida*.

Circular motion. The circular motion of bacteria near surfaces was previously reported for *E. coli* both at air–liquid (27) and solid–liquid interfaces (58, 63) and for *P. putida* at solid–liquid interfaces (33, 64). Counterintuitively, despite their very different flagellar arrangements (Fig. 1*A* and *SI Appendix*, Fig. S1 and Table S1), circular patterns were also observed here for *P. putida*, to a lesser extent for *E. coli*, and for *V. natriegens* (Fig. 2 *C* and *D*). Theoretically, the hydrodynamic interactions between a flat surface and a bacterium swimming on a parallel plane to it are indeed able to explain this curved pattern of trajectories (58, 60).

In summary, in quasi-open spaces, such as plazas, when the movement is limited only by parallel vertical or horizontal walls placed at distances considerably larger than the size of bacteria, their motility can be approximately characterized as stable movement parallel to the wall, wall escapers, or—rarely—as wall accumulators, as derived from bacterial geometric parameters and hydrodynamics-based modeling of the movement near surfaces of monotrichous bacteria.

Motility in Tightly Confining Geometries.

Motility in linear channels. Following the experiments in plazas with high and low ceilings and to avoid (to the extent possible) the impact on motility from more than two vertical walls, further experiments used only microfluidic channels with a 6 μm distance between the horizontal planes.

Overall motility characteristics; sinusoidal movement. When laterally confined in wider channels (e.g., 6 to 8 μm), *V. natriegens* and *E. coli* showed the strongest propensity for moving along walls (Fig. 4*A* and *SI Appendix*, Fig. S10 for 3D trajectories), correlating well with their motility behavior in plazas (Fig. 2*A* and *B*) and their movement parallel to the vertical (Fig. 2*C* and *D*) and horizontal walls (*SI Appendix*, Fig. S9).

P. putida exhibited an apparent sinusoidal movement, especially in larger channels (Fig. 4*A*). A Fast Fourier Transform (FFT) analysis of the trajectories (*SI Appendix*, Figs. S11 and S12*B*) indicated that *V. natriegens*, *V. fischeri*, and, to a much lesser extent, *E. coli* also present sinusoidal movement characteristics, with wavelengths increasing roughly proportionally with an increase in channel widths (*SI Appendix*, Fig. S12*B*). It was demonstrated (39, 65) that monotrichous wall escapers (with this behavior being predicted, partially, for *P. putida* in Fig. 3) move in distorted helical paths in channels of large rectangular transversal section. This upwards correlation between motility wavelengths and available volume for movement is similar to the larger radii of the circular movement in plazas with higher ceilings than in those with low ceilings (Fig. 2*C* and *SI Appendix*, Fig. S5*C*). *M. marinus* also exhibited sinusoidal-like behavior, but the FFT analysis showed that this movement is only the result of frequent collisions to, and bouncing from, the walls.

In narrower channels (i.e., 3 to 6 μm), the tighter confinement increasingly forced bacteria to move along the channel axis (except for *M. marinus*) rather than exhibited their motility behavior observed in open spaces (plazas). Moreover, in tighter (but still larger than the lateral size of the cell) channels, bacterial movement appeared to benefit from both hydrodynamics and steric interaction with the walls, which synergistically push bacteria in the same direction due to the lateral-only confinement of straight channels (66).

Velocities in channels. Analysis of the velocities in straight channels appeared to further substantiate the synergy between hydrodynamics-driven and steric interactions–driven motility mechanisms. Indeed, while *M. marinus* exhibited a moderate decrease in average velocity with the decrease of the width of the channel, including compared with that in the plazas, due to an increase in collisions with the walls, all other species did not show any notable and systemic velocity variation with channel widths (*SI Appendix*, Fig. S13). Furthermore, the double histograms of the velocity in channels (Fig. 4*B*, for rectangular 6 × 6 μm channels; full analysis in *SI Appendix*, Fig. S14) revealed that *V. natriegens* and *E. coli* presented a distinctive bimodal distribution of velocities at the walls, with one velocity higher and one lower than the overall velocity. This bimodal distribution, for the species with the lowest ratios of the cell body and of the flagella (a_1/a_2 and $L/\bar{a}$, respectively, Fig. 3 and *SI Appendix*, Table S2), could be the result of separate instances of short-term cell adhesion to the wall and movement acceleration due to the steric interaction of flagella with the walls. In this context, it was reported (67) that the interaction between the walls and the flagella of *E. coli* translates into a "thrusting aid" for those bacteria running smoothly along solid surfaces. It was also reported, for *E. coli* (30, 68), *B. subtilis* (69), and *S. marcescens* (29), that bacteria exhibited higher velocities in narrower channels (which eventually decreases significantly in even narrower channels, due to the severe mechanical constraints applied to the cells), which is supported by the bimodal distribution of velocities observed for *E. coli* (and *V. natriegens*) here.

Straight versus U-turn movements. In straight channels, bacterial motility was expected to be increasingly driven by steric interactions, to the detriment of hydrodynamics, with a decrease in channel widths. This increased impact of the steric interactions can explain the species-specific proportion of U-turns (Fig. 4*C*). First, the species with the lowest ratio of flagellum/length/cell body (i.e., *V. natriegens* and *E. coli*) (Fig. 3) had the lowest overall proportion of U-turns, with an apparent decrease of U-turns with the channel width for the larger *E. coli* (Fig. 4 *C*, *Bottom*). Conversely, the species clustered at higher characteristic values of $L/\bar{a}$ and a_1/a_2 ratios (i.e., *P. putida* and *V. fischeri*) (Fig. 3) have a considerably higher proportion of U-turns than *V. natriegens* and *E. coli*, and there was even a considerably higher proportion for *V. fischeri* (Fig. 4*D*, fourth from the top). Second, *M. marinus*, with its characteristic frequent collisions and rebounds from the walls, had a low ratio of U-turns, with the notable exception of the 2 μm–wide channels. This unique behavior can be explained by the extreme steric interactions of *M. marinus* with both walls in channels with 2 μm widths, (i.e., as large as the cell body) (Fig. 4*D*, second from the top), resulting in the bacterial cell being "pinned" by both vertical walls then "flipped" in the 6 μm–tall vertical plane of the channel, followed by the movement in the opposite direction. Third, *P. putida*, experiencing intermittent wall contact, exhibited a similar ratio of U-turns as *V. natriegens* and *E. coli*. Fourth, *V. fischeri*, which swim the closest to the wall (Fig. 2*B*), had the highest ratio of U-turns.

In summary, these results demonstrate that, when a strong and complex coupling exists between the interaction by parallel walls placed at distances similar to the dimensions of bacteria, their motility is primarily governed by the local steric interactions between the walls and the flagella and, in extreme confinement, the cell body. Consequently, the increase in confinement with narrower

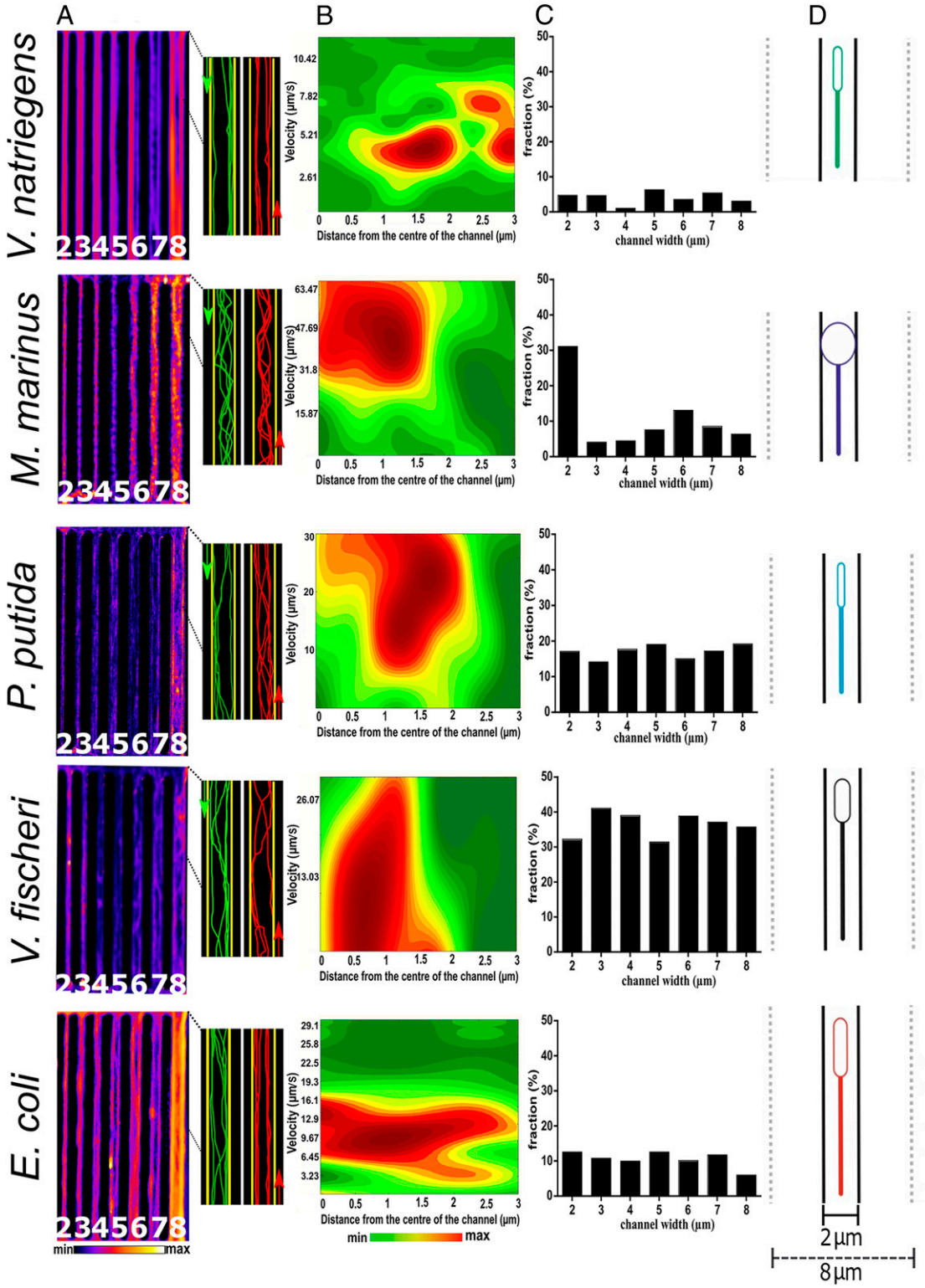

Fig. 4. Bacterial motility in linear channels. (*A*, *Left*) Density maps of the movement patterns of bacteria in channels with different widths. (*A*, *Right*) Bacterial trajectories in 8 μm wide channels, moving from one direction (green) or from an opposite one (red). (*B*) Double histograms of velocity (*y*-axis) versus normalized distance from the center of the linear channel (channel wall on the extreme right) for 6 μm × 6 μm channels (the full analysis is presented in *SI Appendix*, Fig. S14). *E. coli* and *V. natriegens* present a specific bimodal distribution of velocities near the wall. (*C*) Influence of the channel width on the fraction of U-turns. By rows, from top to bottom, are the following: *V. natriegens* (average count of bacteria each frame, $n = 20$/frame); *M. marinus* ($n = 10$/frame); *P. putida* ($n = 19$/frame); *V. fischeri* ($n = 18$/frame); and *E. coli* ($n = 22$/frame). (*D*) Graphical representation of the top view of a bacterium with their average dimensions, in linear channels. The thick and dotted lines represent the minimum and maximum channel widths. Movie S2 presents bacterial movement in channels, with representative trajectories (similar to *A*, *Right*).

channels leads to a decrease in hydrodynamics-based propulsion, and the dilution, or outright disappearance of the classes of motility behavior observed in open spaces.

Motility in channels with angled exits. In the structures with angled exits (Fig. 1*C*, lower right of the fourth image from the left), all bacterial species had a large preference for moving in straight trajectories along the middle axis of the channel, as qualitatively suggested by the density maps (Fig. 5*A*), by representative trajectories (Fig. 5*B* and Movie S3), and by representative bacterial 3D trajectories (*SI Appendix*, Fig. S15). Even for the smallest exit angle (i.e., 30°), the probability of movement in a straight line instead of exiting laterally (estimated as the ratio between bacteria moving straight and the total number that arrived at that intersection) ranges from 72% (for *P. putida*) to 58% (for *M. marinus*). While the general trend for all bacteria was that the exiting probability decreased with increasing exit angle, there were some species-specific details (Fig. 5*C*). First, *V. natriegens*, *E. coli*, and *P. putida* had a clearly decreasing exiting probability with an increase in exit angle, while for *V. fischeri* this trend was less visible, and *M. marinus* exhibited a rather indifferent relationship between exit probabilities and exit angles, following an abrupt drop at angles higher than 30°. Second, all species other than *M. marinus* had a relatively higher exiting probability at 90° angles.

This species-specific motility behavior in angled channels appeared to be the result of bacterial movement being driven by both local hydrodynamics and by steric interactions with the walls. First, the decrease of exit probabilities with exit angles for all species, but especially for *V. natriegens* and *E. coli*, resembles the lower frequency of turning by large angles in open spaces (*SI Appendix*, Fig. S3). The deflection angles in open spaces (*SI Appendix*, Figs. S3 and S4) are near-instantaneous measurements, and while longer integration times would lead to larger apparent values, this could also incorporate other sudden changes of direction, thus obscuring the inherent propensity of bacteria for sideways movement. With this qualification, it is reasonable to expect a connection between the propensity to escape laterally at set angles in angled channels (Fig. 5*C*) and the deflection angles in open spaces. However, this similarity had notable limitations (e.g., all species studied had negligible probabilities of deflection angles at much lower angles than those for bacteria in the angled channels). Second, while the wide spread of deflection angles in plazas (*SI Appendix*, Figs. S3 and S16) for *P. putida* could justify its relatively wide spread of exit probabilities in angled channels, *E. coli*, which had a narrow distribution of deflection angles, had a considerably larger and wider distribution of exit probabilities in angled channels than *P. putida*. Similarly, while both *V. natriegens* and *V. fischeri* exhibited a monotone decrease of frequency with increasing deflection angles in plazas (*SI Appendix*, Figs. S3 and S16), this behavior translated into a monotone decrease of exit probabilities in angled channels only for the former, whereas the latter did not show any obvious correlation between exit probabilities and respective escape angles. Finally, *M. marinus* had a monotone decrease of frequency with increasing deflection angles (after 10°) but an approximately flat relationship between the exit probabilities and escape angles (after 30°).

These observations suggest that, in addition to species-specific hydrodynamics-driven spread of deflection angles in open spaces (plazas), another mechanism was also responsible for determining the exit probabilities in angled channels. Indeed, the species that exhibited a notable departure from the expected extrapolation of behavior in open spaces is also the species whose dimensions exceed the clearance in the angled channels (i.e., *E. coli* and *V. fischeri*) (Fig. 5*D*). Conversely, the species whose dimensions did not surpass the clearance in the angled channels (i.e., *V. natriegens* and *P. putida*) are also those which exhibited a reasonable extrapolation of deflection angles in open spaces to a monotonical decrease of exit probabilities with escape angles. The frequent collisions and bouncing of *M. marinus* had the effect of leveling the exit probabilities regardless of the escape angles (except for 30°, for which there is enough turning space and therefore a higher exit probability, Fig. 5*D*).

It must be also noted that the confinement at the intersection between central and lateral channels did not fully correlate with the respective exit angle. For instance, the 150° exit offered the largest volume available for movement at the intersection between the axial and lateral channels (highlighted in *SI Appendix*, Fig. S2), thus making the comparison with U-turns (at 180°) in tight linear channels, with no variation of widths, inconsistent. Finally, the relatively higher escape probabilities for 90° angles could be the result of smaller free volume at the intersection of the axial channel, with steric interactions biasing bacteria toward lateral exits.

In conclusion, bacterial motility studies in angled channels revealed that when the level of confinement is low, due to the large volume at cross-intersection in relation to smaller bacterial sizes, the movement is mostly driven by hydrodynamics, as an extension of the behavior observed in open spaces. Conversely, when the confinement is tight, due to larger bacterial sizes, the local steric interactions between flagella and the walls contribute substantially to the motility behavior.

Motility in meandered channels. The trapping of bacteria in purposefully designed microfluidics structures is of special interest to various applications [e.g., single-cell genomics (70) and accelerated evolution (71)], and therefore, the responsible mechanisms were studied (72, 73).

The meandered system comprised three channels, each with a different gap between the edge of the "teeth" (i.e., 5 μm [left], 10 μm [middle], and 15 μm [right]) (Fig. 1*C*, lower right, fourth image from left). The tightly confined, 5 μm–wide meandered channels made the motility of all species more complex (Fig. 6 and *SI Appendix*, Fig. S17 and Movie S4). The elastic-like collisions of *M. marinus* resulted in frequent trappings and, consequently, a considerably lower overall "success rate" (defined as the ratio of bacterial entries versus exits, at steady state) than the rest of the bacterial species (Fig. 6*C*). In addition, the 90°-angled corners appeared to operate as traps for *E. coli* and to a lesser extent for *V. natriegens* (bright spots in the density maps in Fig. 6*A*; the higher retention time for *E. coli*, *SI Appendix*, Tables S3 and S4).

Intriguingly, all species appeared to have difficulty in passing the middle, 10 μm–wide channels (Fig. 6*C*). All species made U-turns or carried out repeated deflection at different angles, as well as being trapped (*SI Appendix*, Fig. S18). Intuitively, the overall bacterial velocity in meandered channels is the lowest when compared with those in plazas and straight channels (*SI Appendix*, Fig. S19). However, perhaps counterintuitively, the larger-than–5 μm distance between the walls made the trapping effect of the 90°-angled corners more effective, to a near-total extent for *V. natriegens* and *E. coli* and to a lower relative extent for *V. fischeri*, *M. marinus*, and *P. putida*. As expected, the highest passage "success rate" was provided by the meandered channels with the largest distance between walls (Fig. 6*C*). Again, *M. marinus* and *P. putida* executed more zigzagged trajectories than *V. natriegens*, *V. fischeri*, and *E. coli* (Fig. 6*B*).

This complex and species-specific behavior can be explained in view of previous findings as follows. In channels with large gaps between comb teeth, all bacteria can negotiate the passage, their movement being driven mostly by hydrodynamics, with only occasional interference of the local steric interactions between the flagella and the walls. Conversely, in channels with tight confinement, bacteria are also capable of successfully negotiating the channels, this time "channeled" by the local steric interaction between flagella and the 90°-angled walls. Finally, in the channels in the mesoscale region (i.e., 10 μm distance between the "comb teeth"), the mechanism based on hydrodynamics and that based on the local steric interaction do not operate synergistically,

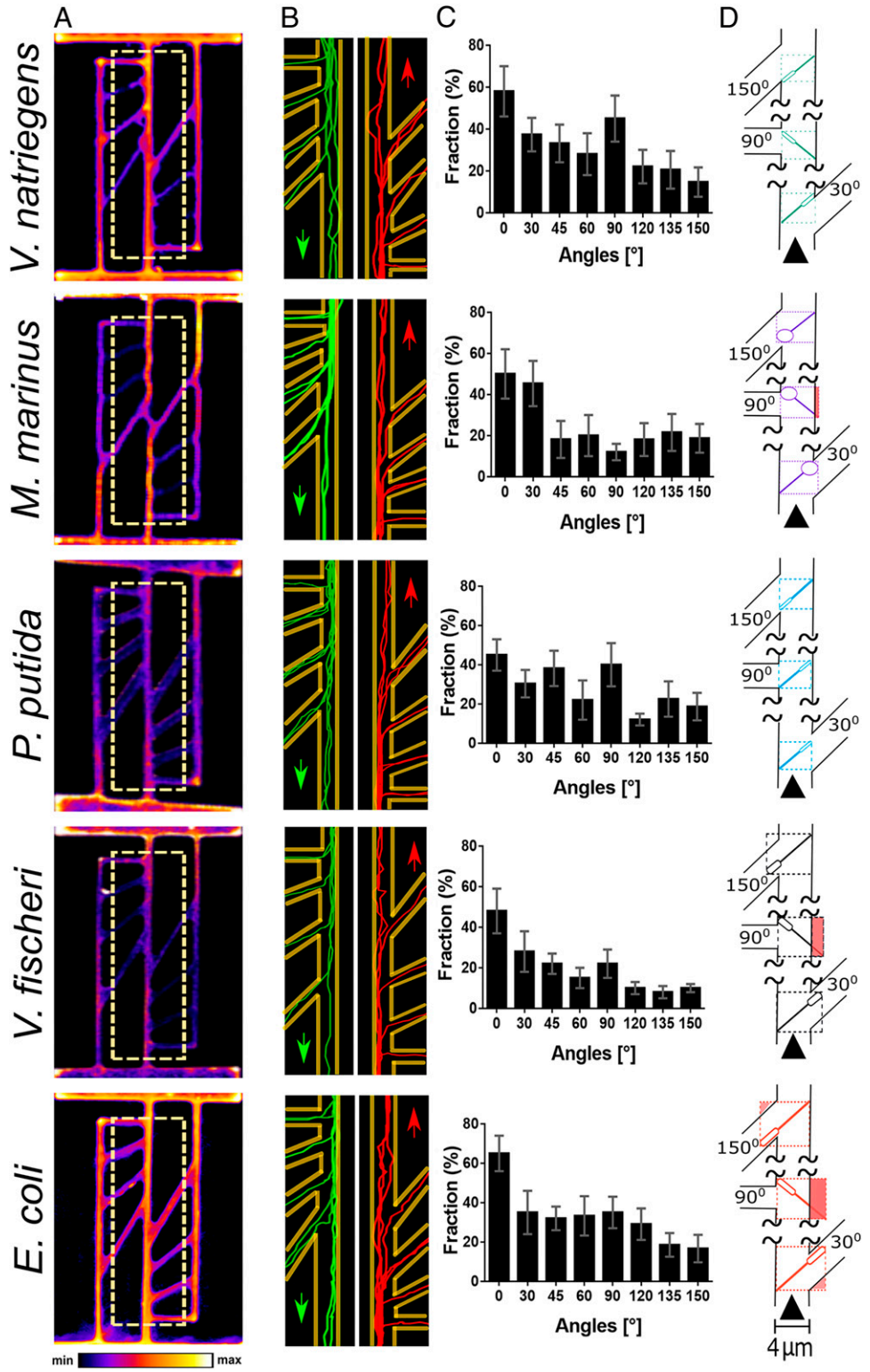

Fig. 5. Bacterial motility in channels with angled exits. (*A*) Density maps of the movement patterns of bacteria in straight parallel channels, connected by side channels at angles ranging from 0° to 150°. All channels are nominally 4 μm wide. (*B*) Bacterial trajectories, either from top (green) or from the opposite direction (red). (*C*) Frequencies of bacteria moving at different exit angles. By rows, from top to bottom, are the following: *V. natriegens* (average count of bacteria each frame, $n = 10$/frame); *M. marinus* ($n = 8$/frame); *P. putida* ($n = 10$/frame); *V. fischeri* ($n = 13$/frame); and *E. coli* ($n = 11$/frame). (*D*) Graphical representation of the top view of bacterium with average dimensions in the angled channels (few representative angles). The areas in light brown represent spaces that exceed the dimensions of the respective bacteria in the respective position. Movie S3 presents bacterial movement in angled networks and representative trajectories (similar to *A*, *Right*).

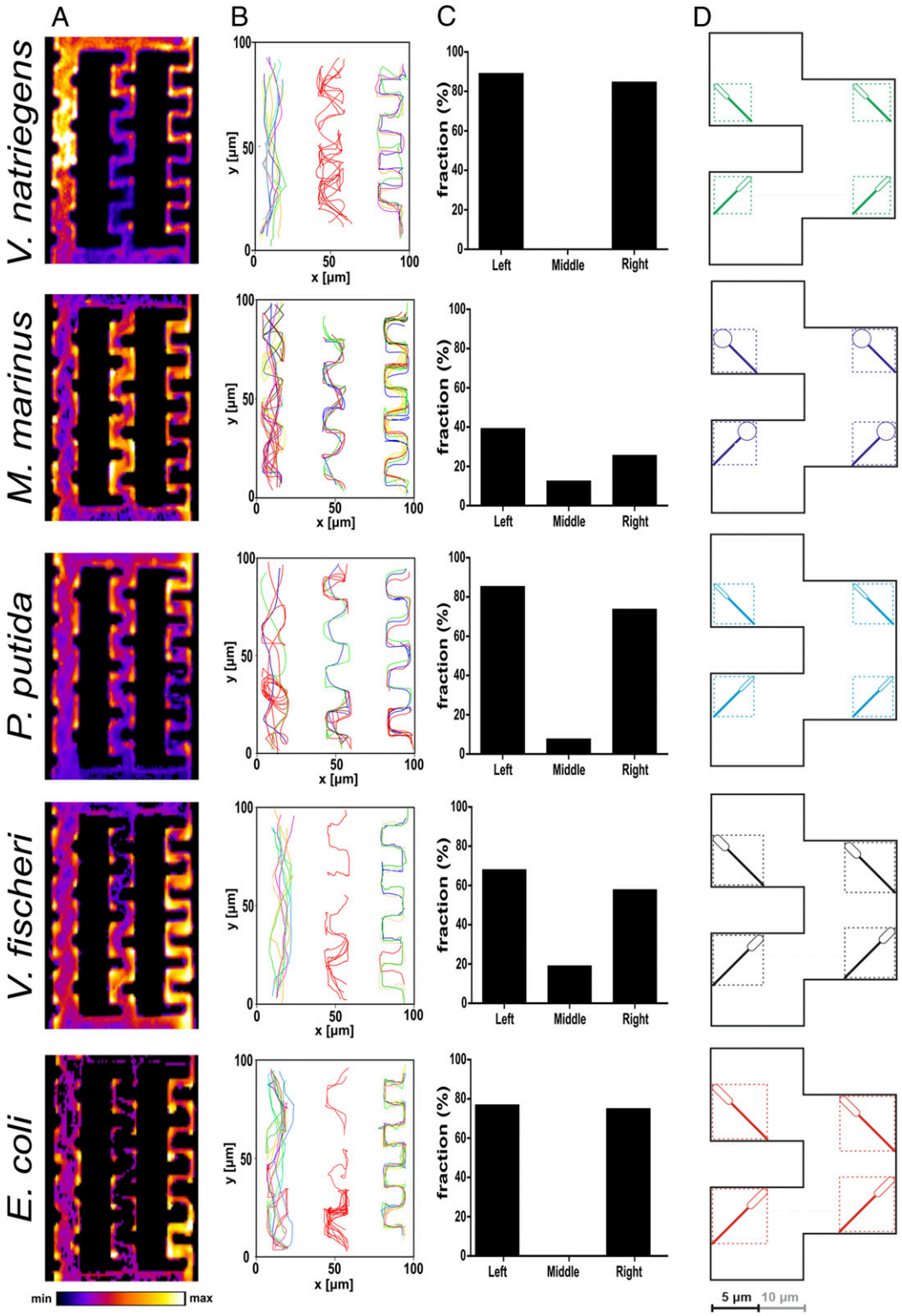

Fig. 6. Bacterial motility in meandered channels. (*A*) Density maps of the bacterial movement patterns. (*B*) Representative tracks of the bacterial motility (trajectories in red are for bacteria that took U-turns or got trapped). (*C*) Frequency of bacteria making successful exits, relative to those that are trapped, or performed U-turns (unsuccessful tracks) for each meandered channel. By rows, from top to bottom, are the following: *V. natriegens* (average count of bacteria each frame, $n = 18$/frame); *M. marinus* ($n = 12$/frame); *P. putida* ($n = 22$/frame); *V. fischeri* ($n = 25$/frame); and *E. coli* ($n = 19$/frame). (*D*) Graphical representation of the top view of bacteria in the mesoscale-sized channel. Movie S4 presents bacterial movement in comb-like channels and representative trajectories (similar to *B*).

increasing the chaotic character of motility and making the overall forward advancement difficult. This is particularly obvious for *V. natriegens* and *E. coli*, which swim parallel to walls (Fig. 3) at a ~2 µm distance from the walls (Fig. 2*B*), thus leading to frequent U-turns. Additionally, these two species are those with the lowest ratios of the cell body and of the flagella (Fig. 3

and *SI Appendix*, Table S2). The more compact architectures of *V. natriegens* and *E. coli* could explain the near-perfect trapping by frequent circular movements in very confined spaces leading to long retention times. Conversely, but for different reasons, *V. fischeri* (a species swimming the closest to the walls, Fig. 2*B*) and *P. putida* (a species with opportunistic distribution in free volumes) can avoid, to a larger extent than *V. natriegens* and *E. coli*, being trapped in the meandered channels. Tellingly, these two species are also those with the highest ratios of the cell body and of the whole bacterium (Fig. 3 and *SI Appendix*, Table S2). This dichotomy of behavior for species swimming parallel to the walls suggests that the steric interactions–driven movement in tight confinement is also modulated by bacterial shape and not only by size (presented schematically in Fig. 6*D*). Indeed, *V. natriegens* and *E. coli* are both very effectively trapped in mesoscale-sized meandered channels, and while *P. putida*, a much shorter species (*SI Appendix*, Table S2), appeared to have some success, *V. fischeri*, the largest of the species swimming parallel to the walls, had the best success rate. Finally, *M. marinus* was also found to exit mesoscale meandered channels more, but its frequent collision-and-rebound on the walls led to slightly lower trapping efficiencies.

To elucidate whether the trapping effect is permanent or transient, the average duration for successfully traversing the meandered channels was quantified (*SI Appendix*, Table S3). Within the experimental time window (4 to 5 min), *V. natriegens* and *E. coli* were unable to successfully traverse the middle-meandered channels. Although *M. marinus* had a shorter retention time due to its high velocity, the distance that it needed to travel in order to be able to exit the meandered channel was longer. Representative 3D trajectories in meandered channels are presented in *SI Appendix*, Fig. S17. The color-coded trajectories for U-turns, successful passages, and trapped bacteria are presented in *SI Appendix*, Fig. S18.

To conclude, in complex geometries, such as meandered channels, hydrodynamics-driven motility is prevalent in wider channels, and the local steric interactions–based mechanism governs bacterial motility in narrow channels. However, in the mesoscale region, these two mechanisms do not act in synergy, resulting in trapping bacteria, with high efficiency for species swimming parallel to the walls, finely modulated by their characteristic shape ratios.

Perspectives and Future Work. The present study, in which we studied a wide range of bacterial motility behavior, provides insights in several areas of applications, as well as suggesting further research.

Fundamentals of bacterial motility mechanics in microenvironments. It was previously shown that a fundamental understanding of the mechanics of the movement of monoflagellated (32, 33, 39) and even biflagellated (61) bacteria in simple geometries, such as the proximity to a surface, can accurately predict motility patterns of bacteria. However, the current study, which described motility patterns of more complex bacterial architectures and in more complex geometries, revealed the limits of this understanding, which would be critical for designing microdevices manipulating bacteria for biosensing, drug delivery, cell sorting, or biocomputation. Further theoretical directions suggested by our study, perhaps coupled with long-term monitoring (74), include analyzing the impact of population variation on cell behavior, investigating the extent to which more complicated bacterial geometries and flagellar arrangements can be represented by more advanced mechanical models, and the need to conduct systematic validation studies. Studies of this type, using artificial microfluidics systems mimicking their natural counterparts, recently carried out for bacteria (75) and fungi (76) or for specifically investigating stochastic processes in bacteria (77), are motivated by the abundance of microbial habitats comprising linear and meandered channels and spaces with different angled turns (*SI Appendix*, Fig. S20).

Motility of magnetic bacteria in biological networks. Chemically or magnetically guided self-propelled bacteria were used for nonsystemic delivery of drugs and cargoes in tumor therapy (78–81). The targeted physiological regions (e.g., deep enteric tissues, hypoxic tumors, tissue granules, and arterioles) (78, 82) are essentially impenetrable to probing devices, but they can be accessed, in principle, by robust bacteria operating as autonomous microrobots moving in the natural microfluidic vascular system (78). The description of bacterial motility, in particular that of *M. marinus*, in PDMS microfluidic channels mimicking the microvascular system surrounding the tumor (e.g., micrometer-range sizes and relevant mechanical elasticity) can lead to the optimization of the operation of these microrobots outside clinical settings, which are expensive to operate and unable to provide reproducible observations at the microscale and in real time.

Bacterial cell sorting. The efficient characterization, sorting, or selection of individual bacterial cells in small volumes are achieved in various microfluidics-based applications, such as those derived from the classical flow cytometry (83–85) to the more recent single-cell analysis (70). In fact, microfluidic devices have been increasingly used for assessing bacterial chemotaxis (86–89), motility (29, 30, 90, 91), and for bacterial cell sorting (46, 72, 91–93), and our results can offer insights for the design of these devices. For instance, the characterization of bacteria as wall accumulators, or wall escapers, can suggest entirely different geometries for microfluidic structures for bacterial cell sorting. Similarly, microfluidic channels can be designed so as to increase retention time (e.g., by having helical profiles) or to amplify the differences in mechanical responses to flow in microfluidics-based flow cytometry.

Network-based biocomputation. Microfluidics-based approaches to computation of problems intractable to electronic computers have been proposed for clique problem (94) and subset sum problem (95). These biological computers require the independent exploration of microfluidic networks encoding a mathematical problem by autonomous agents such as beads (94), cytoskeletal filaments (95), or microorganisms (96). The precision of the microfluidics-based computation is determined by the capacity of biological agents, such as bacteria, to faithfully follow the movement rules embedded in the logic junctions they visit (97). Consequently, the selection of bacterial candidates and the designs of computational microfluidic networks will require the removal or at least minimization of errors, such as U-turns in narrow channels, as well as optimization of the angles of logic gates channels.

Conclusion

We here provided a comprehensive account of the motility of individual bacterial cells, belonging to five species with considerably varied dimensions and morphologies, in microfluidic networks and with various levels of confinement and complexity. For lesser-confining geometries, such as facing one limiting wall, the motility behavior of the five species studied can be assimilated, with qualifications, to that of monotrichous bacteria with similar dimensions. However, when increasing confinement complexity, as for instance in straight channels with various widths, in networks with exits at various angles, and meandered channels, the classification as swimming parallel to the walls for *V. natriegens*, *E. coli*, *V. fischeri*, and *P. putida* and as escapers, partially, for *E. coli*, *P. putida*, and *M. marinus* is increasingly inaccurate, as a result of the increase of the impact of local steric interaction of species-specific morphology with the tightly confining geometry. The study can be also used as a methodological template for the optimization of the design of microfluidic devices with specific functions (e.g., motility-based cell selection for single-cell genomic screening, detection of rare cells, bacterial entrapment devices for diagnostics, or biocomputation).

Materials and Methods

All experimental, modeling, and simulation data analysis protocols are presented in *SI Appendix*.

Data Availability. All study data are included in the article and/or supporting information.

ACKNOWLEDGMENTS. This work was financially supported by the Defense Advanced Research Projects Agency under grant agreements HR0011-16-2-0028 and N66001-03-1-8913, by the Natural Sciences and Engineering Research Council of Canada under grant agreements RGPIN-2016-05019 and RGPIN-2018-04418, by the New Frontiers Research Fund of Canada under grant agreement NFRFE-2019-00129, by the Czech Science Foundation under grant agreement GACR, project 17-11851Y, and by Australian Research Council Future Fellowship FT180100698. We thank the researchers from the Facility for Electron Microscopy Research at McGill University, from the Faculty of Dental Medicine at the University of Montreal, and from the Department of Geology of the University of Quebec at Montreal, for help in electron microscopy characterization of bacteria.

1. A. A. Salyers, D. D. Whitt, *Bacterial Pathogenesis: A Molecular Approach* (ASM Press, Washington, DC, 1994), vol. 3.
2. N. Woodford, D. M. Livermore, Infections caused by gram-positive bacteria: A review of the global challenge. *J. Infect.* **59** (suppl. 1), S4–S16 (2009).
3. P. P. Nagarkar, S. D. Ravetkar, M. G. Watve, Oligophilic bacteria as tools to monitor aseptic pharmaceutical production units. *Appl. Environ. Microbiol.* **67**, 1371–1374 (2001).
4. M. G. Gareau, P. M. Sherman, W. A. Walker, Probiotics and the gut microbiota in intestinal health and disease. *Nat. Rev. Gastroenterol. Hepatol.* **7**, 503–514 (2010).
5. T. A. Harper *et al*., Bioaerosol sampling for airborne bacteria in a small animal veterinary teaching hospital. *Infect. Ecol. Epidemiol.* **3** (2013).
6. S. L. Kandel, N. Herschberger, S. H. Kim, S. L. Doty, Diazotrophic endophytes of poplar and willow for growth promotion of rice plants in nitrogen-limited conditions. *Crop Sci.* **55**, 1765–1772 (2015).
7. Y. Asada, J. Miyake, Photobiological hydrogen production. *J. Biosci. Bioeng.* **88**, 1–6 (1999).
8. A. Esmaeili, A. A. Pourbabaee, H. A. Alikhani, F. Shabani, E. Esmaeili, Biodegradation of low-density polyethylene (LDPE) by mixed culture of Lysinibacillus xylanilyticus and Aspergillus Niger in soil. *PLoS One* **8**, e71720 (2013).
9. M. Höckenreiner, H. Neugebauer, L. Elango, Ex situ bioremediation method for the treatment of groundwater contaminated with PAHs. *Int. J. Environ. Sci. Technol.* **12**, 285–296 (2015).
10. F. Reith, C. M. Zammit, S. L. Rogers, D. C. McPhail, J. Brugger, Potential utilisation of micro-organisms in gold processing: A review. *Miner. Process. Extr. Metall.* **121**, 251–260 (2012).
11. O. Habimana, A. Semião, E. Casey, The role of cell-surface interactions in bacterial initial adhesion and consequent biofilm formation on nanofiltration/reverse osmosis membranes. *J. Membrane Sci.* **454**, 82–96 (2014).
12. C. Verde, D. Giordano, C. M. Bellas, G. di Prisco, A. M. Anesio, "Polar marine microorganisms and climate change" in *Advances in Microbial Physiology*, R. K. Poole, Ed. (Elsevier, 2016), 69, pp. 187–215.
13. G. H. Wadhams, J. P. Armitage, Making sense of it all: Bacterial chemotaxis. *Nat. Rev. Mol. Cell Biol.* **5**, 1024–1037 (2004).
14. A. Z. Komaromy *et al*., Arrays of nano-structured surfaces to probe the adhesion and viability of bacteria. *Microelectron. Eng.* **91**, 39–43 (2012).
15. A. Persat *et al*., The mechanical world of bacteria. *Cell* **161**, 988–997 (2015).
16. O. Felfoul, S. Martel, Assessment of navigation control strategy for magnetotactic bacteria in microchannel: Toward targeting solid tumors. *Biomed. Microdevices* **15**, 1015–1024 (2013).
17. K. F. Jarrell, M. J. McBride, The surprisingly diverse ways that prokaryotes move. *Nat. Rev. Microbiol.* **6**, 466–476 (2008).
18. M. E. J. Holwill, R. E. Burge, A hydrodynamic study of the motility of flagellated bacteria. *Arch. Biochem. Biophys.* **101**, 249–260 (1963).
19. F. Bai *et al*., Conformational spread as a mechanism for cooperativity in the bacterial flagellar switch. *Science* **327**, 685–689 (2010).
20. F. F. Chevance, K. T. Hughes, Coordinating assembly of a bacterial macromolecular machine. *Nat. Rev. Microbiol.* **6**, 455–465 (2008).
21. K. D. Young, Bacterial morphology: Why have different shapes? *Curr. Opin. Microbiol.* **10**, 596–600 (2007).
22. A. Bren, M. Eisenbach, How signals are heard during bacterial chemotaxis: Protein-protein interactions in sensory signal propagation. *J. Bacteriol.* **182**, 6865–6873 (2000).
23. R. M. Harshey, Bacterial motility on a surface: Many ways to a common goal. *Annu. Rev. Microbiol.* **57**, 249–273 (2003).
24. J. G. Mitchell, K. Kogure, Bacterial motility: Links to the environment and a driving force for microbial physics. *FEMS Microbiol. Ecol.* **55**, 3–16 (2006).
25. P. Denissenko, V. Kantsler, D. J. Smith, J. Kirkman-Brown, Human spermatozoa migration in microchannels reveals boundary-following navigation. *Proc. Natl. Acad. Sci. U.S.A.* **109**, 8007–8010 (2012).
26. K. Drescher, J. Dunkel, L. H. Cisneros, S. Ganguly, R. E. Goldstein, Fluid dynamics and noise in bacterial cell-cell and cell-surface scattering. *Proc. Natl. Acad. Sci. U.S.A.* **108**, 10940–10945 (2011).
27. L. Lemelle, J. F. Palierne, E. Chatre, C. Place, Counterclockwise circular motion of bacteria swimming at the air-liquid interface. *J. Bacteriol.* **192**, 6307–6308 (2010).
28. H. C. Berg, L. Turner, Chemotaxis of bacteria in glass capillary arrays. Escherichia coli, motility, microchannel plate, and light scattering. *Biophys. J.* **58**, 919–930 (1990).
29. M. Binz, A. P. Lee, C. Edwards, D. V. Nicolau, Motility of bacteria in microfluidic structures. *Microelectron. Eng.* **87**, 810–813 (2010).
30. B. Libberton, M. Binz, H. van Zalinge, D. V. Nicolau, Efficiency of the flagellar propulsion of Escherichia coli in confined microfluidic geometries. *Phys. Rev. E* **99**, 012408 (2019).
31. D. Giacché, T. Ishikawa, T. Yamaguchi, Hydrodynamic entrapment of bacteria swimming near a solid surface. *Phys. Rev. E Stat. Nonlin. Soft Matter Phys.* **82**, 056309 (2010).
32. H. Shum, E. A. Gaffney, D. J. Smith, Modelling bacterial behaviour close to a no-slip plane boundary: The influence of bacterial geometry. *Proc. Royal Soc. Math. Phys. Eng. Sci.* **466**, 1725–1748 (2010).
33. H. Shum, E. A. Gaffney, The effects of flagellar hook compliance on motility of monotrichous bacteria: A modeling study. *Phys. Fluids* **24**, 061901 (2012).
34. A. Acemoglu, S. Yesilyurt, Effects of geometric parameters on swimming of micro organisms with single helical flagellum in circular channels. *Biophys. J.* **106**, 1537–1547 (2014).
35. H. Shum, E. A. Gaffney, Hydrodynamic analysis of flagellated bacteria swimming near one and between two no-slip plane boundaries. *Phys. Rev. E Stat. Nonlin. Soft Matter Phys.* **91**, 033012 (2015).
36. J. Hu, A. Wysocki, R. G. Winkler, G. Gompper, Physical sensing of surface properties by microswimmers–Directing bacterial motion via wall slip. *Sci. Rep.* **5**, 9586 (2015).
37. Y. Park, Y. Kim, S. Lim, Flagellated bacteria swim in circles near a rigid wall. *Phys. Rev. E* **100**, 063112 (2019).
38. E. Lauga, Bacterial hydrodynamics. *Annu. Rev. Fluid Mech.* **48**, 105–130 (2016).
39. H. Shum, E. A. Gaffney, Hydrodynamic analysis of flagellated bacteria swimming in corners of rectangular channels. *Phys. Rev. E Stat. Nonlin. Soft Matter Phys.* **92**, 063016 (2015).
40. E. K. Sackmann, A. L. Fulton, D. J. Beebe, The present and future role of microfluidics in biomedical research. *Nature* **507**, 181–189 (2014).
41. J. Zhang *et al*., Fundamentals and applications of inertial microfluidics: A review. *Lab Chip* **16**, 10–34 (2016).
42. D. Erickson, D. Q. Li, Integrated microfluidic devices. *Anal. Chim. Acta* **507**, 11–26 (2004).
43. G.-X. Zheng *et al*., An integrated microfludic device for culturing and screening of Giardia lamblia. *Exp. Parasitol.* **137**, 1–7 (2014).
44. C.-X. Xu, X.-F. Yin, Continuous cell introduction and rapid dynamic lysis for high-throughput single-cell analysis on microfludic chips with hydrodynamic focusing. *J. Chromatogr. A* **1218**, 726–732 (2011).
45. D. Yuan *et al*., Sheathless separation of microalgae from bacteria using a simple straight channel based on viscoelastic microfluidics. *Lab Chip* **19**, 2811–2821 (2019).
46. L. Y. Yeo, H. C. Chang, P. P. Chan, J. R. Friend, Microfluidic devices for bioapplications. *Small* **7**, 12–48 (2011).
47. T. Kalisky, S. R. Quake, Single-cell genomics. *Nat. Methods* **8**, 311–314 (2011).
48. R. U. Sheth, S. S. Yim, F. L. Wu, H. H. Wang, Multiplex recording of cellular events over time on CRISPR biological tape. *Science* **358**, 1457–1461 (2017).
49. B. J. Kim, M. Wu, Microfluidics for mammalian cell chemotaxis. *Ann. Biomed. Eng.* **40**, 1316–1327 (2012).
50. K. L. Hanson *et al*., Fungi use efficient algorithms for the exploration of microfluidic networks. *Small* **2**, 1212–1220 (2006).
51. M. Held, A. P. Lee, C. Edwards, D. V. Nicolau, Microfluidics structures for probing the dynamic behaviour of filamentous fungi. *Microelectron. Eng.* **87**, 786–789 (2010).
52. J. Wang *et al*., Detection of size spectrum of microalgae cells in an integrated underwater microfluidic device. *J. Exp. Mar. Biol. Ecol.* **473**, 129–137 (2015).
53. Z. Liu, K. D. Papadopoulos, Unidirectional motility of Escherichia coli in restrictive capillaries. *Appl. Environ. Microbiol.* **61**, 3567–3572 (1995).
54. G. S. Kijanka, I. K. Dimov, R. Burger, J. Ducrée, Real-time monitoring of cell migration, phagocytosis and cell surface receptor dynamics using a novel, live-cell opto-microfluidic technique. *Anal. Chim. Acta* **872**, 95–99 (2015).
55. M. Nayak, A. S. Perumal, D. V. Nicolau, F. C. M. J. M. Van Delft, Bacterial motility behaviour in sub-ten micron wide geometries" in *2018 16th IEEE International New Circuits and Systems Conference*, R. Izquierdo, A. Miled, Eds. NEWCAS 2018 (Montreal, QC, 2018), pp. 382–384.
56. A. S. Perumal, M. Nayak, V. Tokárová, O. Kašpar, D. V. Nicolau, "Space partitioning and maze solving by bacteria" in *Proceedings of the lecture Notes of the Institute for Computer Sciences, Social-Informatics and Telecommunications Engineering, LNICST*, A. Compagnoni, W. Casey, Y. Cai, B. Mishra, Eds. (Pittsburgh, PA, 2019), pp. 175–180.
57. A. P. Berke, L. Turner, H. C. Berg, E. Lauga, Hydrodynamic attraction of swimming microorganisms by surfaces. *Phys. Rev. Lett.* **101**, 038102 (2008).
58. E. Lauga, W. R. DiLuzio, G. M. Whitesides, H. A. Stone, Swimming in circles: Motion of bacteria near solid boundaries. *Biophys. J.* **90**, 400–412 (2006).
59. E. P. Ipina, S. Otte, R. Pontier-Bres, D. Czerucka, F. Peruani, Bacteria display optimal transport near surfaces. *Nat. Phys.* **15**, 610–615 (2019).
60. A. S. Utada *et al*., Vibrio cholerae use pili and flagella synergistically to effect motility switching and conditional surface attachment. *Nat. Commun.* **5**, 4913 (2014).
61. H. Shum, Microswimmer propulsion by two steadily rotating helical flagella. *Micromachines (Basel)* **10**, 65 (2019).
62. K. Bente *et al*., High-speed motility originates from cooperatively pushing and pulling flagella bundles in bilophotrichous bacteria. *eLife* **9**, e47551 (2020).
63. W. R. DiLuzio *et al*., Escherichia coli swim on the right-hand side. *Nature* **435**, 1271–1274 (2005).
64. M. Theves, J. Taktikos, V. Zaburdaev, H. Stark, C. Beta, Random walk patterns of a soil bacterium in open and confined environments. *EPL* **109**, 28007 (2015).
65. H. Shum, "Simulations and modelling of bacterial flagellar propulsion," PhD thesis, University of Oxford, Oxford, UK (2011).
66. S. Bianchi, F. Saglimbeni, R. Di Leonardo, Holographic imaging reveals the mechanism of wall entrapment in swimming bacteria. *Phys. Rev. X* **7**, 011010 (2017).

67. P. D. Frymier, R. M. Ford, H. C. Berg, P. T. Cummings, Three-dimensional tracking of motile bacteria near a solid planar surface. *Proc. Natl. Acad. Sci. U.S.A.* **92**, 6195–6199 (1995).
68. N. Figueroa-Morales *et al*., E. coli "super-contaminates" narrow ducts fostered by broad run-time distribution. *Sci. Adv.* **6**, eaay0155 (2020).
69. J. Männik, R. Driessen, P. Galajda, J. E. Keymer, C. Dekker, Bacterial growth and motility in sub-micron constrictions. *Proc. Natl. Acad. Sci. U.S.A.* **106**, 14861–14866 (2009).
70. P. C. Blainey, The future is now: Single-cell genomics of bacteria and archaea. *FEMS Microbiol. Rev.* **37**, 407–427 (2013).
71. B. M. Paegel, G. F. Joyce, Microfluidic compartmentalized directed evolution. *Chem. Biol.* **17**, 717–724 (2010).
72. P. Galajda, J. Keymer, P. Chaikin, R. Austin, A wall of funnels concentrates swimming bacteria. *J. Bacteriol.* **189**, 8704–8707 (2007).
73. T. V. Phan *et al*. Bacterial route finding and collective escape in mazes and fractals. *Phys. Rev. X* **10**, 031017 (2020).
74. F. K. Balagaddé, L. You, C. L. Hansen, F. H. Arnold, S. R. Quake, Long-term monitoring of bacteria undergoing programmed population control in a microchemostat. *Science* **309**, 137–140 (2005).
75. H. Massalha, E. Korenblum, S. Malitsky, O. H. Shapiro, A. Aharoni, Live imaging of root-bacteria interactions in a microfluidics setup. *Proc. Natl. Acad. Sci. U.S.A.* **114**, 4549–4554 (2017).
76. M. Held, O. Kašpar, C. Edwards, D. V. Nicolau, Intracellular mechanisms of fungal space searching in microenvironments. *Proc. Natl. Acad. Sci. U.S.A.* **116**, 13543–13552 (2019).
77. L. Potvin-Trottier, S. Luro, J. Paulsson, Microfluidics and single-cell microscopy to study stochastic processes in bacteria. *Curr. Opin. Microbiol.* **43**, 186–192 (2018).
78. S. Martel, Swimming microorganisms acting as nanorobots versus artificial nanorobotic agents: A perspective view from an historical retrospective on the future of medical nanorobotics in the largest known three-dimensional biomicrofluidic networks. *Biomicrofluidics* **10**, 021301 (2016).
79. S. Martel, C. C. Tremblay, S. Ngakeng, G. Langlois, Controlled manipulation and actuation of micro-objects with magnetotactic bacteria. *Appl. Phys. Lett.* **89**, 233904(2006).
80. H. Terashima, S. Kojima, M. Homma, Flagellar motility in bacteria structure and function of flagellar motor. *Int. Rev. Cell Mol. Biol.* **270**, 39–85 (2008).
81. D. Akin *et al*., Bacteria-mediated delivery of nanoparticles and cargo into cells. *Nat. Nanotechnol.* **2**, 441–449 (2007).
82. S. Martel, Bacterial microsystems and microrobots. *Biomed. Microdevices* **14**, 1033–1045 (2012).
83. B. P. Tracy, S. M. Gaida, E. T. Papoutsakis, Flow cytometry for bacteria: Enabling metabolic engineering, synthetic biology and the elucidation of complex phenotypes. *Curr. Opin. Biotechnol.* **21**, 85–99 (2010).
84. D. Huh, W. Gu, Y. Kamotani, J. B. Grotberg, S. Takayama, Microfluidics for flow cytometric analysis of cells and particles. *Physiol. Meas.* **26**, R73–R98 (2005).
85. J. Oakey *et al*., Particle focusing in staged inertial microfluidic devices for flow cytometry. *Anal. Chem.* **82**, 3862–3867 (2010).
86. X. Wang, J. Atencia, R. M. Ford, Quantitative analysis of chemotaxis towards toluene by Pseudomonas putida in a convection-free microfluidic device. *Biotechnol. Bioeng.* **112**, 896–904 (2015).
87. J. A. Crooks, M. D. Stilwell, P. M. Oliver, Z. Zhong, D. B. Weibel, Decoding the chemical language of motile bacteria by using high-throughput microfluidic assays. *ChemBioChem* **16**, 2151–2155 (2015).
88. H. H. Jeong *et al*., Microfluidic monitoring of Pseudomonas aeruginosa chemotaxis under the continuous chemical gradient. *Biosens. Bioelectron.* **26**, 351–356 (2010).
89. H. Kim, J. Ali, K. Phuyal, S. Park, M. J. Kim, Investigation of bacterial chemotaxis using a simple three-point microfluidic system. *Biochip J.* **9**, 50–58 (2015).
90. O. Sipos, K. Nagy, P. Galajda, Patterns of collective bacterial motion in microfluidic devices. *Chem. Biochem. Eng. Q.* **28**, 233–240 (2014).
91. B. Kaehr, J. B. Shear, High-throughput design of microfluidics based on directed bacterial motility. *Lab Chip* **9**, 2632–2637 (2009).
92. S. Park, D. Kim, R. J. Mitchell, T. Kim, A microfluidic concentrator array for quantitative predation assays of predatory microbes. *Lab Chip* **11**, 2916–2923 (2011).
93. Z. Wu, B. Willing, J. Bjerketorp, J. K. Jansson, K. Hjort, Soft inertial microfluidics for high throughput separation of bacteria from human blood cells. *Lab Chip* **9**, 1193–1199 (2009).
94. D. T. Chiu, E. Pezzoli, H. Wu, A. D. Stroock, G. M. Whitesides, Using three-dimensional microfluidic networks for solving computationally hard problems. *Proc. Natl. Acad. Sci. U.S.A.* **98**, 2961–2966 (2001).
95. D. V. Nicolau Jr *et al*., Parallel computation with molecular-motor-propelled agents in nanofabricated networks. *Proc. Natl. Acad. Sci. U.S.A.* **113**, 2591–2596 (2016).
96. D. V. Nicolau *et al*., Molecular motors-based micro- and nano-biocomputation devices. *Microelectron. Eng.* **83**, 1582–1588 (2006).
97. F. C. M. J. M. van Delft *et al*., Something has to give: Scaling combinatorial computing by biological agents exploring physical networks encoding NP-complete problems. *Interface Focus* **8**, 20180034 (2018).

SUPPORTING INFORMATION

Patterns of bacterial motility in microfluidics-confining environments

*Viola Tokárová, Ayyappasamy Sudalaiyadum Perumal, Monalisha Nayak, Henry Shum, Ondřej Kašpar, Kavya Rajendran, Mahmood Mohammadi, Charles Tremblay, Eamonn Andrew Gaffney, Sylvain Martel, Dan V. Nicolau Jr., Dan V. Nicolau**

1. Detailed Experimental Section

1.1. Experimental protocols

1.1.1. *Bacterial species*

Five bacterial species living in micro-environments were studied, presented here in an increased order of architectural complexity. *Vibrio natriegens* is a rod-shaped, polar uni-flagellated bacterium.(1, 2) *Magnetococcus marinus* (MC-1) is a spherical bacterium with two clusters of seven flagella at one polar end (3, 4), *Pseudomonas putida* (ATCC® 12633™) (5, 6) and *Vibrio fischeri* (Ward's Science 15-5722) have rod-shaped bodies,(7, 8) and are polar-multi-flagellated bacteria. *Escherichia coli* MG1665 (K12-wild type) is a rod-shaped bacterium with a peritrichous flagellar machinery.(9-12) **Figure 1** (main text) and **Table S1** present the characteristics of the five bacterial strains used in this study, and **Figure S1** presents detailed SEM images of individual bacterial cells.

All the cultures, except *M. marinus*, were maintained in agar plates and cultured in Luria-Bertani (LB) medium prior to the experiments. *P. putida* and *V. fischeri* were cultivated at room temperature (RT), as reported elsewhere (5) while *E. coli* and *V. natriegens* were cultivated at 30ºC. *E. coli* and *V. natriegens* were genetically transformed with a plasmid to express mCherry for visualization and tracking in microfluidic devices. *E. coli* and *V. natriegens* were transformed to constitutively express the plasmid pMF440-mChe (a gift from Dr. Michael Franklin's lab, Addgene Plasmid #62550). The plasmids express mCherry, a red fluorescent protein in bacteria to visualize them in our experiments using fluorescence microscopy techniques. *M. marinus* was cultivated and maintained at École Polytechnique de Montréal, Canada, in a microaerophilic, chemo-hetero lithotrophic chemically-defined medium, rich with ferrous ions, grown in dark, at room temperature, as described earlier (3), while a 24 hrs to 48 hrs culture was used for microfluidic experiments.

1.1.2. *Design and fabrication of the microfluidics networks*

The microfluidic chip for probing bacterial motility (**Figure 1C**, first left) comprises parallel reservoirs with widths of 2 mm, connected through 1 mm-wide 'bus' channel (**Figure 1C**, second left). Every area consists of 1 mm x 1 mm structures of 5 x 5 identical geometries separated by open spaces ('plazas') of 100 µm x 100 µm (**Figure 1C**, third left).

The quantification of specific motility parameters required specific designs of the microfluidic structures **(Figure 1C**, third left, clockwise direction), as follows: (i) a set of linear, 100 µm-long channels (**Figure S2A**) with various widths, i.e., 2, 3, 4, 5, 6, 7 and 8 µm, probed the linear movement and possible U-turns (~ 180°); (ii) zig-zag channels, 'combs', with 5, 10, and 15 µm-long teeth length (**Figure S2C**), presenting 90° angles for each tooth, probed the corner preference and wall guiding behavior; (iii) 3.5 µm-wide channels (**Figure S2B**) presenting different sideways angles, i.e., 0°, 30°, 45°, 60°, 90°, 120°,

135°, and 150°, probed the deflection of movement and turn angle preferences; and (iv) 100 x 100 µm chambers, 'plazas', with two entrances opposite to each other on opposite walls (**Figure S2**).

The microfluidic chip was made of polydimethylsiloxane (PDMS) through the replication of a positive-relief silicon master, fabricated by standard photolithography.(9, 13) The mixture of PDMS and cross-linker (weight ratio 10:1) was poured onto the silicon master, degassed inside vacuum chamber to remove air bubbles, and cured at 65°C overnight to ensure full cross-linking. After cutting and peeling off, the PDMS replica was treated in air plasma for 30 seconds to render the surface hydrophilic, before irreversibly bonding it onto the glass coverslip (also plasma-activated for 30 seconds).

1.1.3. *Impact of the distance between horizontal planes*

In chambers with lateral dimensions considerably larger than the size of bacterial cells, and if the horizontal surfaces are placed at a distance that allows the decoupling of their impact, bacterial motility is limited only by one of the horizontal planes (and by the vertical walls and corners placed at large distances from each other). However, to avoid the sagging, or outright collapse of the top horizontal plane in PDMS microfluidic chambers, the optimal height/width ratio is around 0.05,(14) i.e., approximately 5 µm for a 100x100 µm chamber. Because bacteria approach walls diagonally, a conservative design of the microfluidics structures required that the distance between the horizontal walls be larger than the vertical projection of the bacterium length (cell body and flagella) at a 45° diagonal. For the dimensions of the bacteria studied, this condition was fulfilled, for all species, by a height of 6 µm (**Figure 1A, Table S1**). Conversely, this condition was not fulfilled for any of the species studied at a height of 4 µm, with *E. coli, V. fischeri, M. marinus, P. putida,* and *V. natriegens*, exceeding the 4 µm clearance, in this order (**Figure 1B**).

Indeed, the motility behavior in large chambers with low ceilings presented evidence of the coupling of the impact on both horizontal planes on bacterial motility, i.e., a considerable alteration of the distribution of deflection angles of the 2D projections of bacterial trajectories (**Figures S3**), which appeared to be more pronounced for species with characteristic length larger than the 4 µm clearance. A finer analysis of the bacterial 3D trajectories revealed a much narrower distribution of the curvatures of these trajectories, for all species, for 4 µm tall plazas compared with those in 6 µm tall plazas (**Figure S4**). These streamlined trajectories appear be the result of the increased confinement by both horizontal walls of the chambers with 4 µm heights.

A similar analysis for plazas with 4 µm heights (**Figure S5**) and the characteristic trajectories (presented in **Movie S1**) also showed important differences in the motility behavior of all bacteria. Consequently, more detailed motility experiments were performed extensively in 6 µm-tall microfluidic structures.

1.1.4. *Motility experiments.*

Immediately after sealing the PDMS structure on the coverslip, the microfluidics chip was flooded with the working buffer, i.e., LB medium for *V. natriegens, P. putida*, *V. fischeri*, *E. coli*, and Phosphate-Buffered Saline (PBS) buffer for *M. marinus*, for 1 hour to pre-wet the microfluidic structure, then stored inside a wet chamber at 4°C before use. Separately, a log-phase bacterial suspension was introduced into the microfluidics chamber through the open ends of the PDMS stamps and left in contact for few minutes to allow of bacteria to enter the

channels and plazas (**Figure 1C**, first on the left). To ensure that the bacterial chemotaxis-free motility is the only, or the overriding mechanism at play, the working fluids have an excess of nutrients, and the experimental time is short enough (few minutes inside the confined environment) to ensure that the level of nutrients remains practically constant. Furthermore, the bacterial population in microenvironments never reached the population density of log phase or stationary phase (15, 16), during which other factors, e.g., quorum sensing, or chemotaxis could play a role in space searching and foraging for nutrients.

1.1.5. *Image acquisition and analysis*

Bacterial flagella were stained using Hardy Diagnostics Flagella Stain following the product protocol and visualized by optical microscopy (Olympus IX83, U PLAN S-APO 100X oil objective). The scanning electron microscopy images of bacterial cells and PDMS structures were obtained using a Quanta FEI450 SEM and Hitachi S-3400N SEM system. The image acquisition of *M. marinus* used a specially designed inverted Zeiss AxioImager Z1m microscope with AxioVision Software Sonny HD-1000 camera (with VirtualDub 1.10.4 software), LD Epiplan 20x (NA 0.4) and N-Achroplan 10x (NA 0.25) objectives. The dark field imaging system enhances the contrast between bacterial cell and surrounding structures, which is necessary for further image analysis of fast swimming bacteria such as *M. marinus*. The experiments with *V. natriegens*, *P. putida*, *V. fischeri*, and *E. coli* were performed on a system mounted on an inverted, Spinning Disk Confocal Olympus IX83 microscope, with MetaMorph® Microscopy Automation & Image Analysis Software (Molecular Devices), and 10x (NA 0.4), 20x (NA 0.75) and 40x (NA 0.95) Differential Interference Contrast (DIC) objectives. The duration of image acquisition was based on type of imaging like bright field microscopy (for *M. marinus* MC-1 and *P. putida*) or with fluorescence microscopy (*E. coli*, *V. natriegens*, *V. fischeri*). Depending on the type of acquisition, a different exposure was used, and the frames used for plotting density maps or another trajectory analysis were normalized accordingly. Density maps also used the average number of bacteria per frame.

ImageJ 1.50a (17), a public domain software, has been used for image analysis, density map reconstructions, and time-resolved bacterial tracking. The density maps of bacterial movement inside confined structures were prepared from original RGB image stack as follows: (i) a median of 8-bit image stack (a background) was created using a ‘Z Project’ function; (ii) a new stack was created as a difference between the original stack and the background; (iii) the histogram of a new stack was adjusted and converted to a binary image; (iv) the binary operations ‘Close’ and ‘Dilate’ were applied to remove the remaining noise; and (v) all binary images were superimposed into one image.

In some cases, the density map created by the procedure described above was accompanied by a high level of noise near the walls of the channels, due to the non-uniform light conditions in the optically transparent PDMS chip. In such cases, the original stack of n-images was duplicated in the range of 1 to *n*-1 and 2 to *n*. Thus, the difference |Img2 - Img1| between stacks shifted by one frame highlighted the bacterial movement without the background and light-related noise. This difference, used to calculate the absolute change between two images, is important, since bacteria have also free movement along the vertical z-axis, in and out of the focal plane, in the range limited by the height of the PDMS structures. The new image stack was processed by steps (iii)-(v) described above to create the respective density maps.

The trajectories of the single bacterium were tracked by the automatic (TrackMate, ImageJ), and the manual (MTrackJ, ImageJ) plugins (18). The TrackMate plugin, using LAP tracker

algorithm, was used for *M. marinus*, which exhibits a quasi-linear motion, with low deflection angles (see Results Section 2.1), thus making the analysis amenable to automation. The settings for this 2-parameter tracker were chosen to reach the maximum distance between the two consecutive points of one trajectory, at a given time, with a time gap set to three frames. However, because *P. putida* and *V. fischeri* tend to swim along the walls, thus leading to the possibility of interrupted trajectories, the automatic tracking required more statistical data. The image analysis of these species used the manual MTrackJ plugin, with a dark/white centroid snap feature, with a point-and-click tracking. To facilitate automatic tracking, we used fluorescently labelled *E. coli* and *V. natriegens*. In all cases, the acquired x-y-time coordinates were used for calculating the velocity and the deflection angle from trajectories of individual bacteria. All experiments and image analysis were performed in biological replicates, with at least 3 sets of experiment for each bacterial species in each motility structure. For analysis and probability/fraction % representation, at least 200-300 independent bacterial count were used in multiple sets, to obtain a high confidence data and a statistical significance of $P<0.005$. For the density map, a fixed number of frames with average bacterial count ($n=18\pm7$) on each frame in any particular motility structure for any bacterial species was kept standard, so that the density map intensity was comparable to minimum and maximum values for each motility structure under discussion.

1.1.6. Imaging for mapping 3D motility patterns of bacteria in 6 μm plaza

For imaging bacterial trajectories in 3D, we used the piezo-stage controller of Olympus IX83, confocal microscope for rapid acquisition of z-stacking of the bacterial trajectory. The devices of 6 μm tall plaza were z-stacked at a step size of 2 μm for 12 μm. In total 7 images were captured at an exposure of 10 ms (a total of ~90 ms to 100 ms per time point). For plotting trajectory analysis, the tracking was done manually, followed by the intensity-based segregation of trajectory points for each z-planes with highest fluorescence or bright field intensity.(19) This highest intensity bacterial corresponds to ‘in focus’ bacterial trajectories and marks the z-plane maximum for each time point. We used ‘Origin’ software for plotting the 3D tracks as described in the Results and discussion section.

1.2. Bacterial species

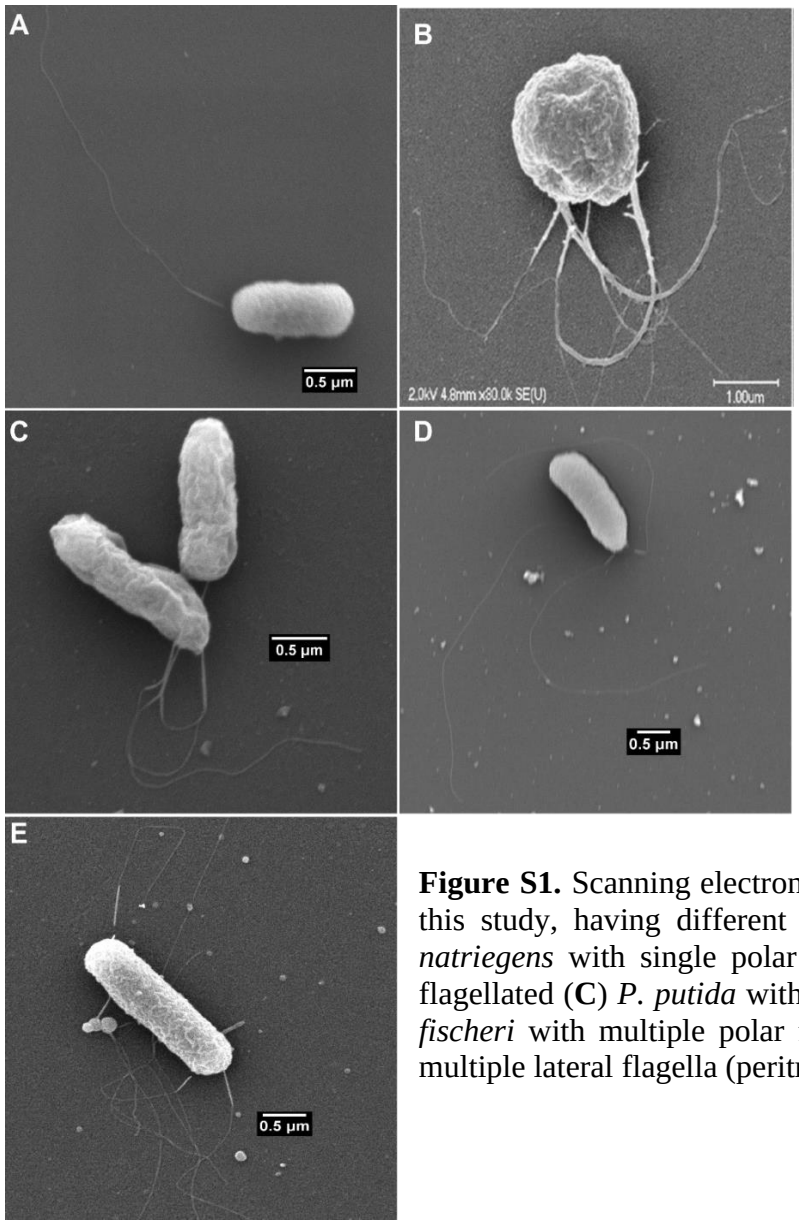

Figure S1. Scanning electron images of the bacteria used in this study, having different flagellar architectures. (**A**) *V. natriegens* with single polar flagella; (**B**) *M. marinus*, bi-flagellated (**C**) *P. putida* with multiple polar flagella; (**D**) *V. fischeri* with multiple polar flagella; (**E**) *E. coli* K12 with multiple lateral flagella (peritrichous arrangement).

Table S1. Characteristics of the motile bacteria used in this study

Bacteria	***V. natriegens***	***M. marinus***	***P. putida***	***V. fischeri***	***E. coli***
Cell: Length [µm] Width [µm]	 1.5 ± 0.5 0.9 ± 0.1	 1.9 ± 0.2 1.9 ± 0.2	 1.6 ± 0.3 0.6 ± 0.2	 1.8 ± 0.1 0.6 ± 0.1	 1.9 ± 0.6 1.0 ± 0.2
Flagellum/-a Architecture Length [µm]	 One 4.7 ± 0.9	 Two bundles 4.0 ± 0.8	 Polar multiple 3.9 ± 0.8	 Polar multiple 5.1 ± 1.1	 Peritrichous 4.7 ± 1.4
Velocity [µm.s^{-1}]	15-20	Up to 200	27 - 44	60-100	< 20
Habitat	Marine, or fresh water	Marine	Soil	Marine (free; or fish, squid)	Ubiquitous, intestine/gut
Aerobic	Aerobic	Micro-aerophilic	Aerobic	Aerobic	Facultative anaerobic
Media	LB, LB-V2 salt medium	Chemo-hetero-lithotrophic	LB broth/agar	LB broth/agar	LB broth/agar

1.3. Microfluidics structures and their characteristic dimensions

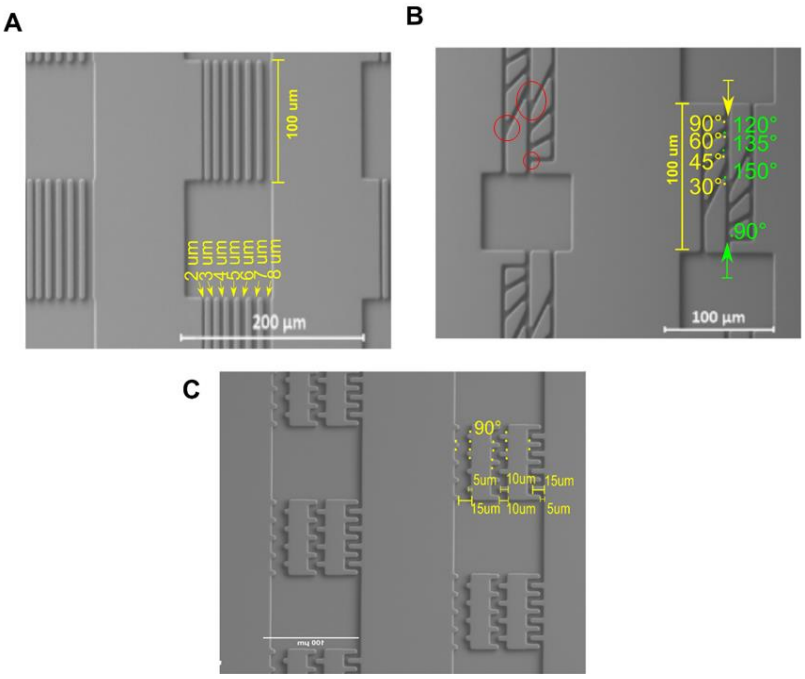

Figure S2. Scanning electron microscopy (SEM) images of PDMS microfluidic structures for the probing of the bacterial motility, separated by quasi-open spaces. **A**. Linear channels with different widths, from 2 µm to 8 µm. **B.** Turn-angle chip presenting eight different angles (0°, or straight path, and 30°, 45°, 60°, 90°, 120°, 135°, and 150° angles). Note the various volumes available for motility at the intersection of the axial and lateral angle, for 90°, 30°/150°, and 150° angles (red circles, top left). **C.** Meandered channels with three different tooth lengths (5 µm, 10 µm, and 15 µm).

2. Results and Discussion

2.1. Motility in large chambers

2.1.1. Impact of the distance between horizontal planes

2.1.1.1. Turn angle preference from 2D trajectories

To assess the possible coupling of the interaction of the horizontal plane in plazas, for 4 and 6 µm heights, respectively, the *turn angle preference* of motility was calculated, in the first instance, using 2D projections of the 3D trajectories (**Figure S3**).

It was found that the turn angle preference was considerably different for plazas with 4 µm, and 6 µm heights, respectively. Importantly, this difference appears to be larger for bacteria whose characteristic lengths are larger than the clearance of 4 µm heights (**Figure 1B**), with the notable exception of *E. coli*.

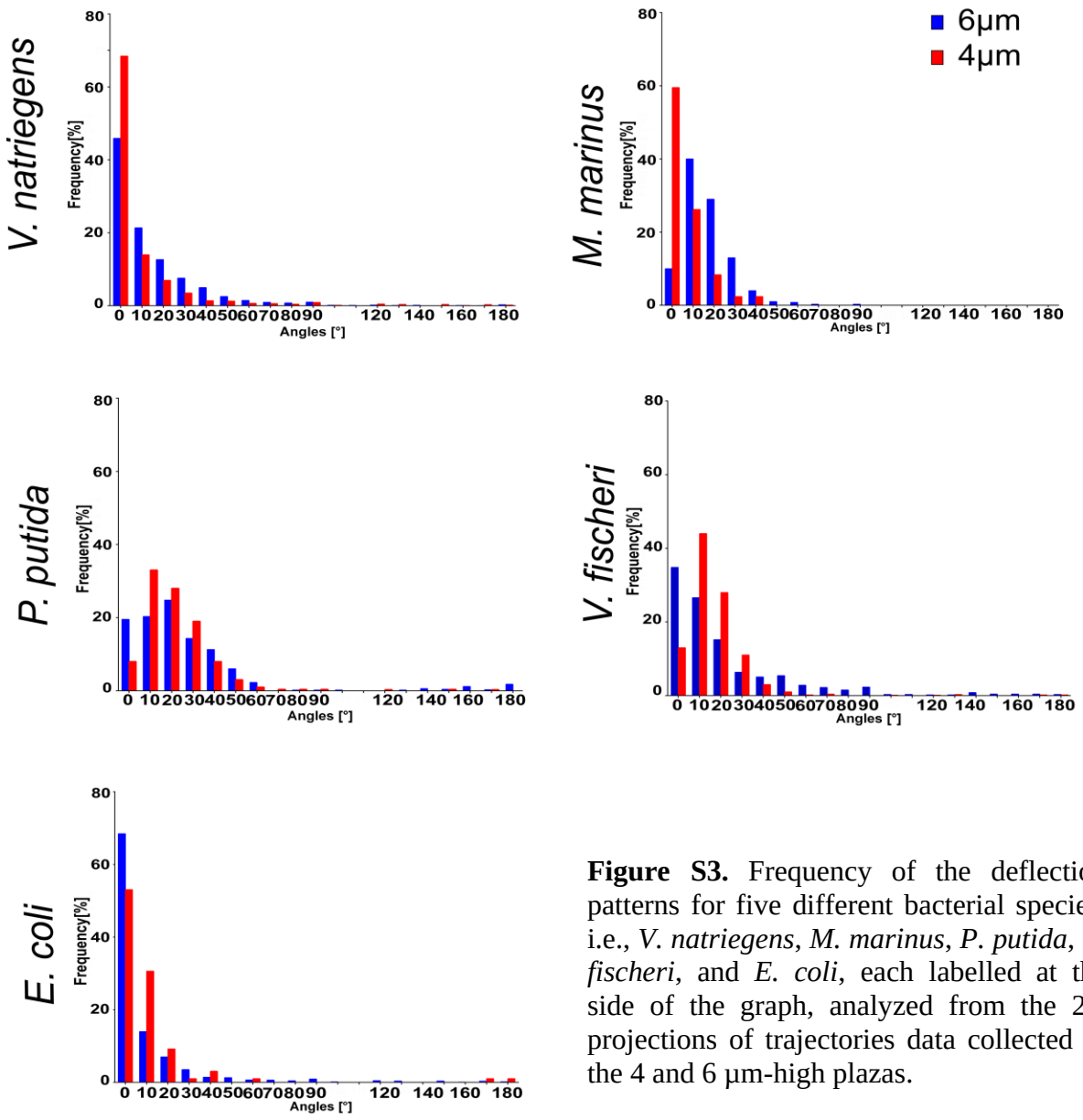

Figure S3. Frequency of the deflection patterns for five different bacterial species, i.e., *V. natriegens*, *M. marinus*, *P. putida*, *V. fischeri*, and *E. coli*, each labelled at the side of the graph, analyzed from the 2D projections of trajectories data collected in the 4 and 6 µm-high plazas.

2.1.1.2. Curvature analysis from 3D trajectories

A finer analysis of the possible coupling of the interaction of the top and bottom horizontal walls of the plazas is possible through the analysis of the representative 3D trajectories. To this end, twenty individual trajectories, each for each plaza with both 6 µm, and 4 µm heights, and for each bacterial species, respectively, were used for *curvature analysis*, with positive values corresponding to clockwise, and negative values corresponding to counterclockwise rotations. The median curvature value was calculated for each trajectory and twenty trajectories of each species and both heights were compared (**Figure S4**), as follows: for parametrized trajectories [x(t),y(t)], the curvature k is

$k(x_0,y_0) = [x_{-1}\cdot y_{-1} - x_1\cdot y_1]/[(x_{-1}^2 + y_{-1}^2)^{3/2}]$, where -1, 0, 1, represent the temporal sequence.

Even a cursory inspection of the distribution of the average curvature for all bacteria showed much streamlined trajectories, that is, the considerably narrower distribution of curvatures, which could be understood only by the constrained applied by both horizontal walls.

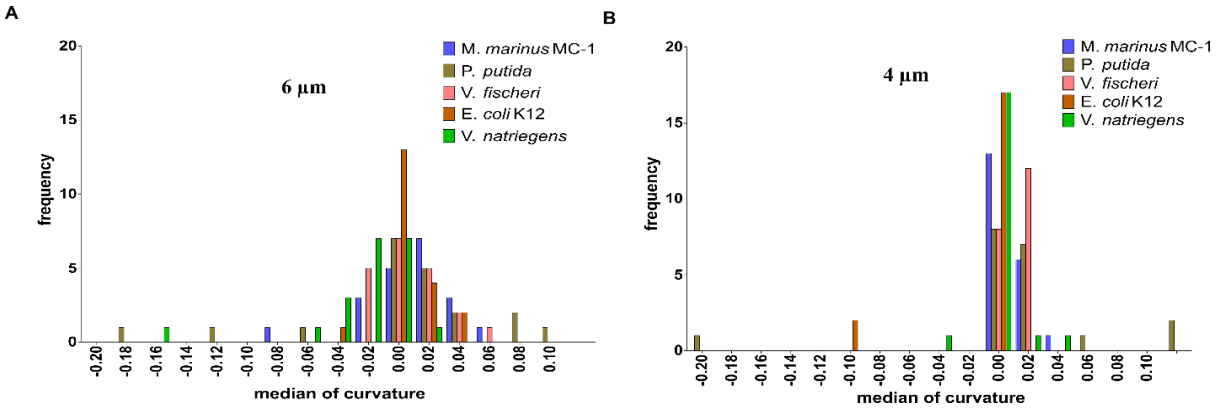

Figure S4. Curvature analysis of trajectories in plazas with 6 µm (A) and 4 µm (B) heights.

2.1.1.3. Preliminary analysis of bacterial motility in 4 µm *tall plazas*

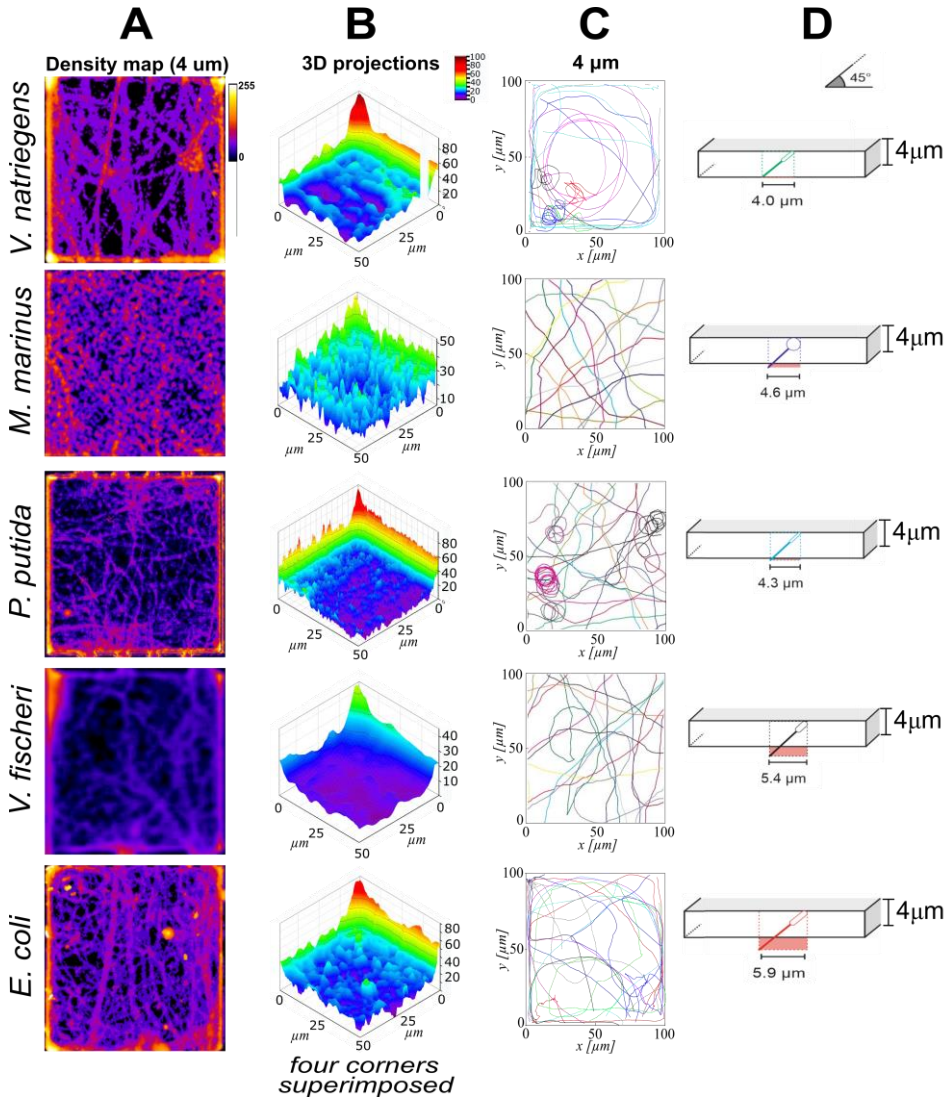

Figure S5. Motility in plazas with 4µm heights. **A**. Density maps of bacterial locations. **B**. Probabilities of bacterial positions. Note the differences in spatial distribution of probabilities compared with those for plazas with 6µm heights**. C.** Characteristic longest trajectories of bacterial motility. Note the differences in trajectory features compared with those for plazas with 6µm heights. **D**. Projection of bacterial length fit across the height of the chamber at 45º.

Detailed explanations for Figure S5: **A**. Density maps of bacterial locations in plazas. Left column; "0 (min)" and "255 (max)" represent the color-coded heat map of no/highest bacterial population, respectively. **B**. Estimation of probabilities of positions, estimated from the 2D projections of the bacterial positions on a horizontal plane, followed by superimposition of the four corners of the density maps of the plaza (similar procedures as in **Figure 2B**, but presented here in 3D). Left column; "0 (blue, min)" and "100 (red, max)" represent the color code for bacterial density along the corners and the walls. **C.** Characteristic longest trajectories of bacterial motility, as 2D projections. **D**. Graphical projection of bacterial length fit across the height of the at 45º. By rows, from top to bottom: *V. natriegens* (average count of bacteria in each frame, n = 14/frame); *M. marinus* (n = 12/frame); *P. putida* (n = 15/frame); *V. fischeri* (n = 15/frame); and *E. coli* (n = 13/frame). Movie S1 presents bacterial overall movement in plazas, and representative trajectories (similar to C). Note the rather considerable difference between the long trajectories (column C) compared with equivalent representation for trajectories in **Figure 2C**.

2.1.2. Overall spatial density.

2.1.2.1. Quantification of bacterial positions at a distance from the horizontal walls in the plazas

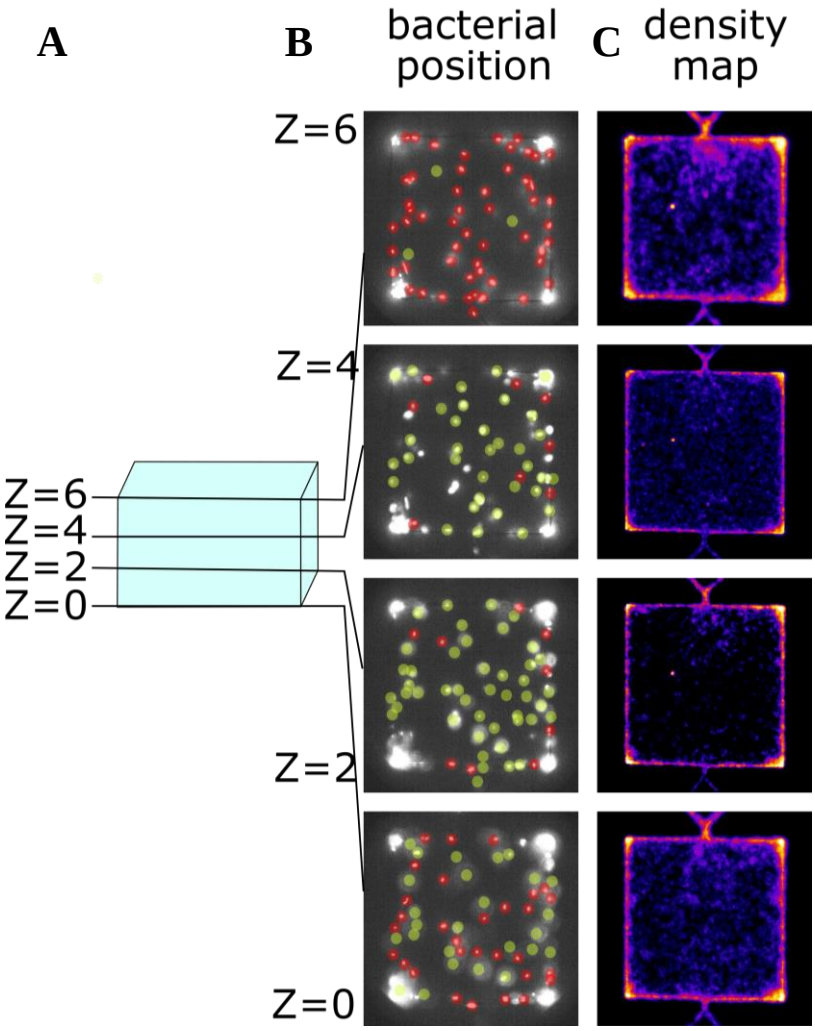

Figure S6. Quantification of bacterial positions using z-stack imaging of the plazas volume (representative analysis for *E. coli*). **A.** Schematic representation of the chamber, with four z-stacked planes, distanced by 2 μm step size. **B**. Assigning of the position of bacteria. The yellow circles over fluorescent signal represent the bacterial species that are out of focal plane, while the red circled overlapped over the fluorescing bacteria represent the bacterial outside the focal planes. **C.** Density maps for the representative z-resolved *E. coli* imaging at different levels. The density maps show that most of bacteria were placed close to the top and bottom horizontal planes.

2.1.2.2. 3D trajectory analysis and z-positioning of five bacterial species in tall plazas.

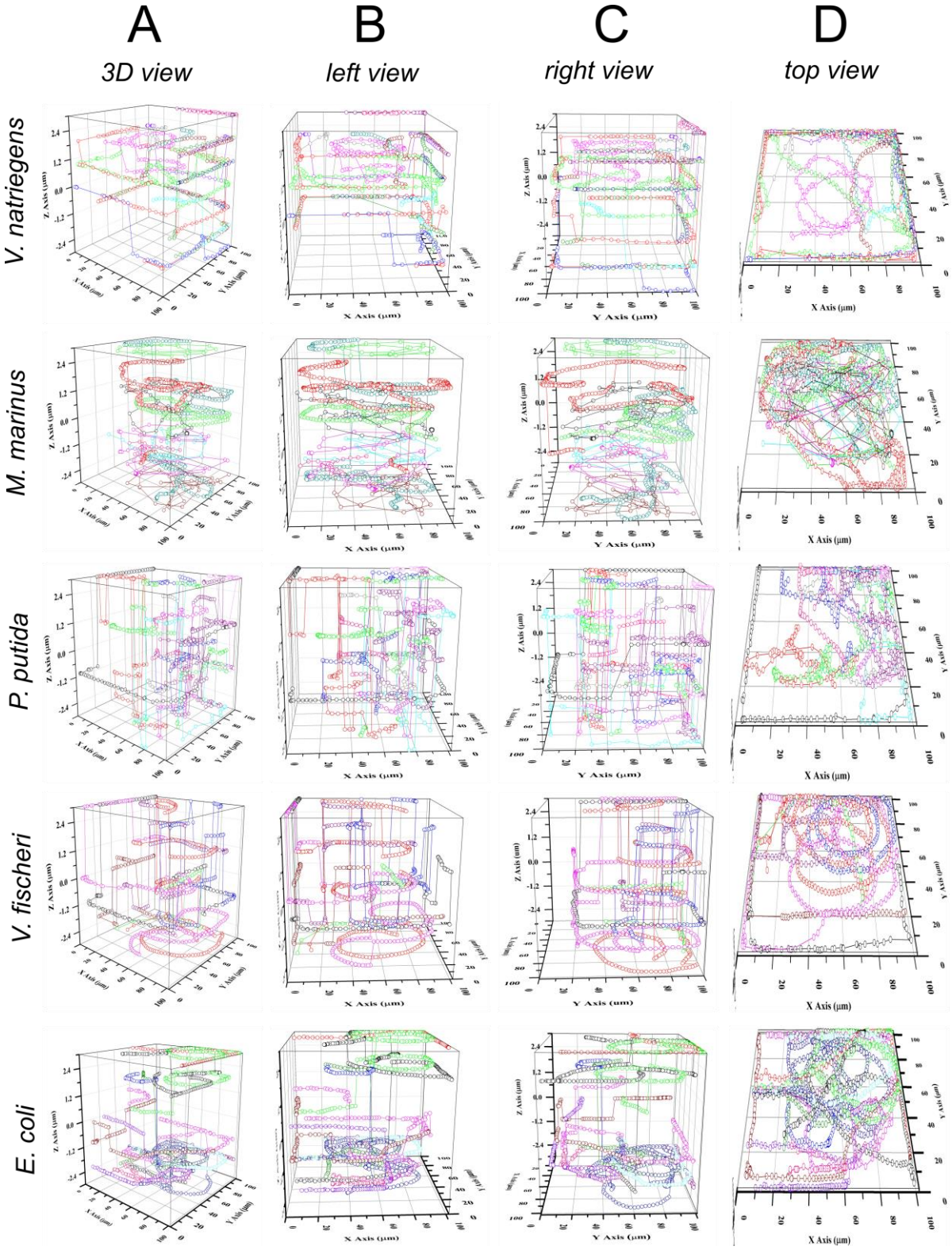

Figure. S7. Representation of bacterial trajectories in 3D using z-stack imaging in plazas. Most of trajectory lengths (density of bacterial positions) were close, and often parallel to the adjacent wall. The transitions between one plane to the opposing one occurred quickly (few points, in few ms). For *M. Marinus* (presenting helical motility patterns) and *P. Putida*, most trajectories were placed away for the horizonal planes, especially in the center for the plaza. Images represent different view angles of the 3D trajectories (complementing **Figure 2D**).

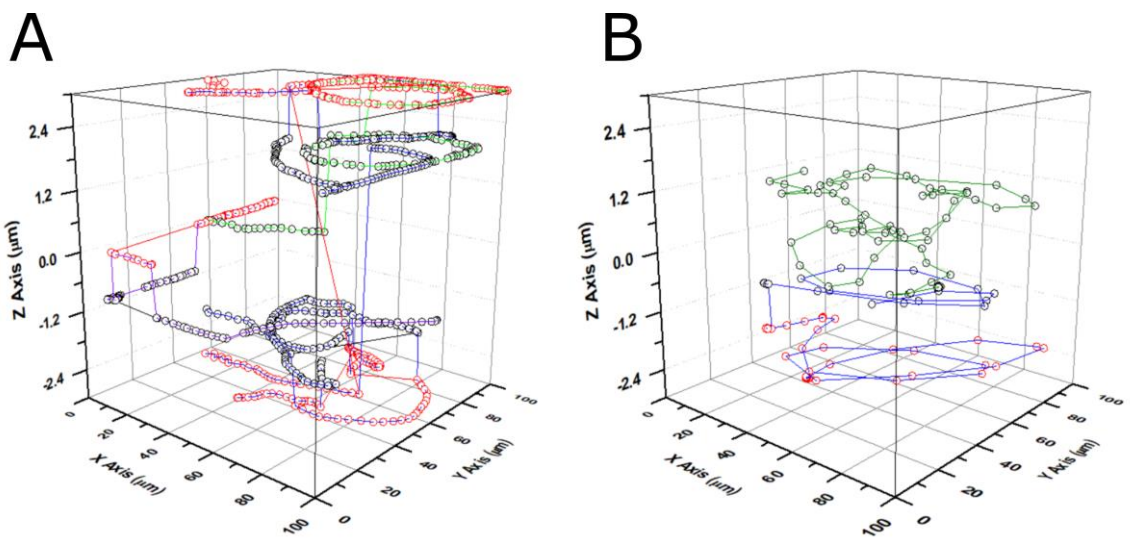

Figure S8. Comparison of two bacterial species with opposite motility behavior. **A**. *E. coli* moves in planes parallel to the walls, at different distances. **B**. *M. marinus* does not move in a parallel plane, thus flipping from a wall accumulator to a wall escaper behavior.

2.1.2.3. Estimation of the distance of swimming parallel to the walls

The first estimation of the distance bacteria swim away from the wall was provided by the "probability map" (**Figure 2B**). This estimation was statistically precise, but it suffered from the edge effects, as the walls the bacteria are swimming near are only 6 µm in width. A fundamentally better (but statistically weaker) option is to collect the z coordinates of the 3D trajectories in the central region of the plazas, i.e., away from edge effects, and then to construct histograms of the bacterial presence away from the horizontal walls (**Figure S9**).

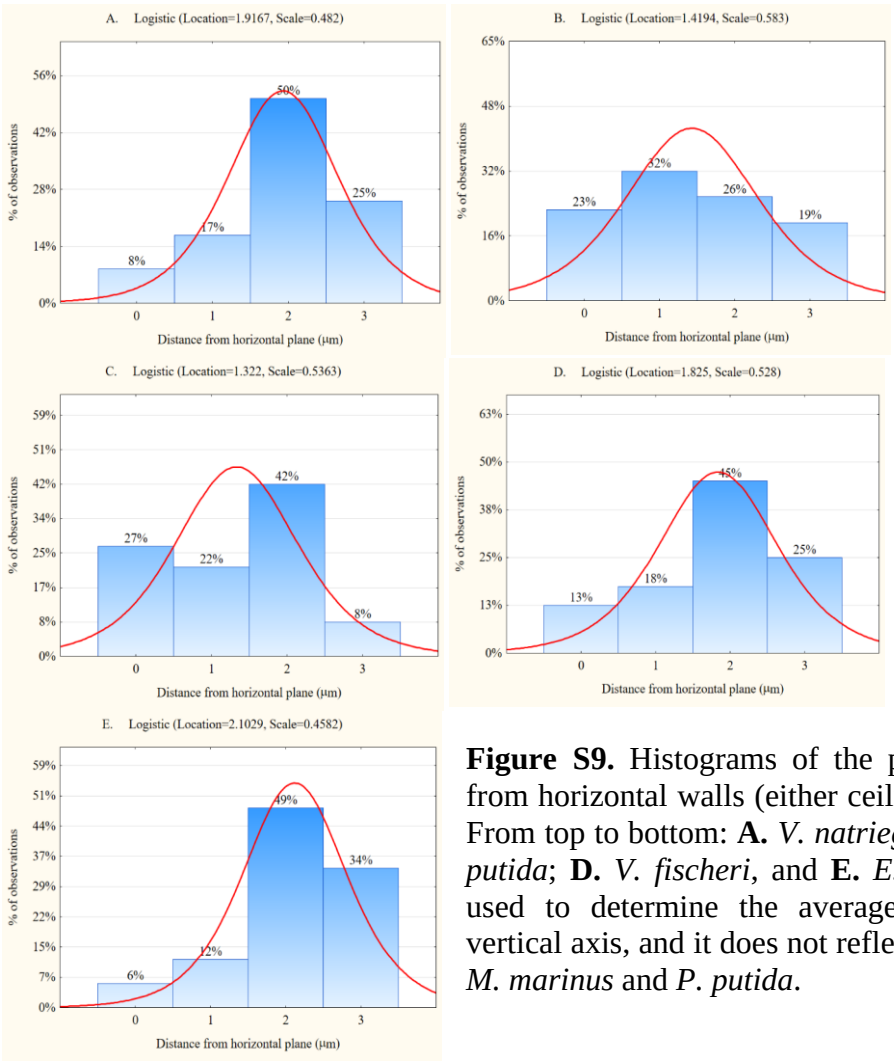

Figure S9. Histograms of the positions of bacteria away from horizontal walls (either ceiling, or floor) of the plazas. From top to bottom: **A.** *V. natriegens;* **B**. *M. marinus;* **C**. *P. putida*; **D.** *V. fischeri*, and **E.** *E. coli*. The logistic fit was used to determine the average bacterial position along vertical axis, and it does not reflect an actual distribution for *M. marinus* and *P. putida*.

2.1.2.4. Simulation of motility of monotrichous bacteria near walls

Numerical results for boundary interactions shown in Figure 3 are upgraded from previous work.(20) The data were generated as follows. A model bacterium is considered consisting of a spheroidal cell body propelled by a single rigidly rotating flagellum. Body and flagellum shapes based on experimental measurements are depicted in Figure 3. The variable $\bar{a}$ is defined as the characteristic length scale of the body. The choice of semi-major axis a_1 and semi-minor axis a_2 of the body result in various aspect ratios a_1/a_2 while maintaining a fixed cell volume $V = (4/3)\pi a_1 a_2^2 = (4/3)\pi \bar{a}^3$. The values of $\bar{a}$ based on cell lengths and widths for the studied bacteria are given in **Table S2**. In addition to the body aspect ratio, the length of the model flagellum is varied, keeping its helical pitch and amplitude fixed.

For each set of geometry parameters, a Boundary Element Method was used to numerically calculate the velocity of the bacterium placed in a given configuration specified by the distance h and orientation angle θ relative to a solid wall. The instantaneous translational and rotational velocities of the bacterium are determined by satisfying the equations of Stokes flow subject to no-slip boundary conditions on the surface of the cell body, flagellum, and wall. The propulsive thrust generated by rotating the flagellum is generally not exactly aligned with the axis of the body, leading to a slight wobbling motion. To determine the average velocity over timescales longer than a motor revolution, the instantaneous velocities was calculated at uniform increments of the angular phase of the flagellum relative to the body and take the mean value. This process allows us to define an average vertical speed $\frac{dh}{dt}$ and rate of turning $\frac{d\theta}{dt}$ that depend on the current h and θ.

For some bacterial shapes, it was found that there is a certain combination of distance and orientation, denoted (h^*, θ^*), at which $\frac{dh}{dt} = 0$ and $\frac{d\theta}{dt} = 0$. This is an equilibrium configuration because the swimmer remains at this height and orientation indefinitely. Moreover, this is a stable equilibrium because bacteria starting at other configurations, provided they are not pointing too sharply away from the surface, would approach the equilibrium point. Bacteria with such an equilibrium point are referred in this study as 'swimmers parallel to wall' because they tend to remain in this plane (which is close to boundaries). This regime is placed at the top right quadrant in Figure 3. The stable configuration was computed for various combinations of the cell body aspect ratio and flagellum length and the stable height h^* was graphically presented by a color scale in the upper right of Figure 3.

As the body aspect ratio decreases (approaching a spherical shape) for a fixed flagellum length, it was found that the stable height decreased until the bacterium became too close to the wall for numerical methods to be reliable. Since these model bacteria also have a strong attraction to walls, in fact descending into walls, they are classified in this study as 'boundary accumulators'. This regime is placed, approximately, at the top left quadrant in Figure 3.

Starting from boundary accumulators with a computed stable configuration, decreasing the flagellum length increases the stable height. There is a region of rapid transition from $h^*/\bar{a} \approx 1$ (where the cell body is very close to the wall) to $h^*/\bar{a} > 5$. Beyond this point, the stable height is far enough from the wall that hydrodynamic interactions are negligible. In this regime, located in the lower portion of Figure 3, the bacteria turn and swim away from the wall even if they are initially approaching the wall, thus referred 'boundary escapers'.

The hydrodynamic explanation for why changes in the geometry of the bacterium affect its motion near walls is that the shape determines the distribution of stresses acting on the cell membrane and flagellum. The flow field generated by a swimming bacterium can be

approximated by combinations of a force dipole, source dipole, and higher order terms that each produce different interactions with a wall.(21) The relative strengths of these terms, and hence the net behavior near walls, depend on the shape of the organism.

Table S2. Characteristic geometrical parameters of the bacteria studied used for the simulation of motility behavior (monotrichous architecture model), as in Figure 3.

Parameter→ Bacteria↓	**a_1/a_2**	**L/ā**	**h*/ā**	**L+a_1 (μm)**
V. natriegens	1.75 ±0.75	9.51 ±3.48	3.05	5.45 ± 2.30
M. marinus	10.2 ±0.21	4.35 ±1.30	1.35	4.95 ± 1.80
P. putida	3.19 ±1.56	10.84 ±5.03	2.47	4.70 ± 1.90
V. fischeri	3.11 ±0.69	12.34 ±4.15	3.73	6.00 ± 3.40
E. coli	2.10 ±1.02	8.64 ±4.33	2.74	5.65 ± 2.30

Legend (32):

a_1 = polar radius of cell body (half the cell length); a_2 = equatorial radius of cell body (half of the diameter diameter); [a_1/a_2] = aspect ratio of the cell body; L = curvilinear length of the flagellum (approximated by the axial length of the flagellum); ā = radius of sphere with volume of cell body; L/ ā = aspect ratio of the bacterium; h* = optimal distance from the wall (for swimmers parallel to the walls), determined in this study from the z-stack analysis (**Figure S9**); and h*/ā = non-dimensional distance from the wall.

2.2. Motility in tightly confining geometries

2.2.1. Motility in linear channels

2.2.1.1. Overall motility characteristics

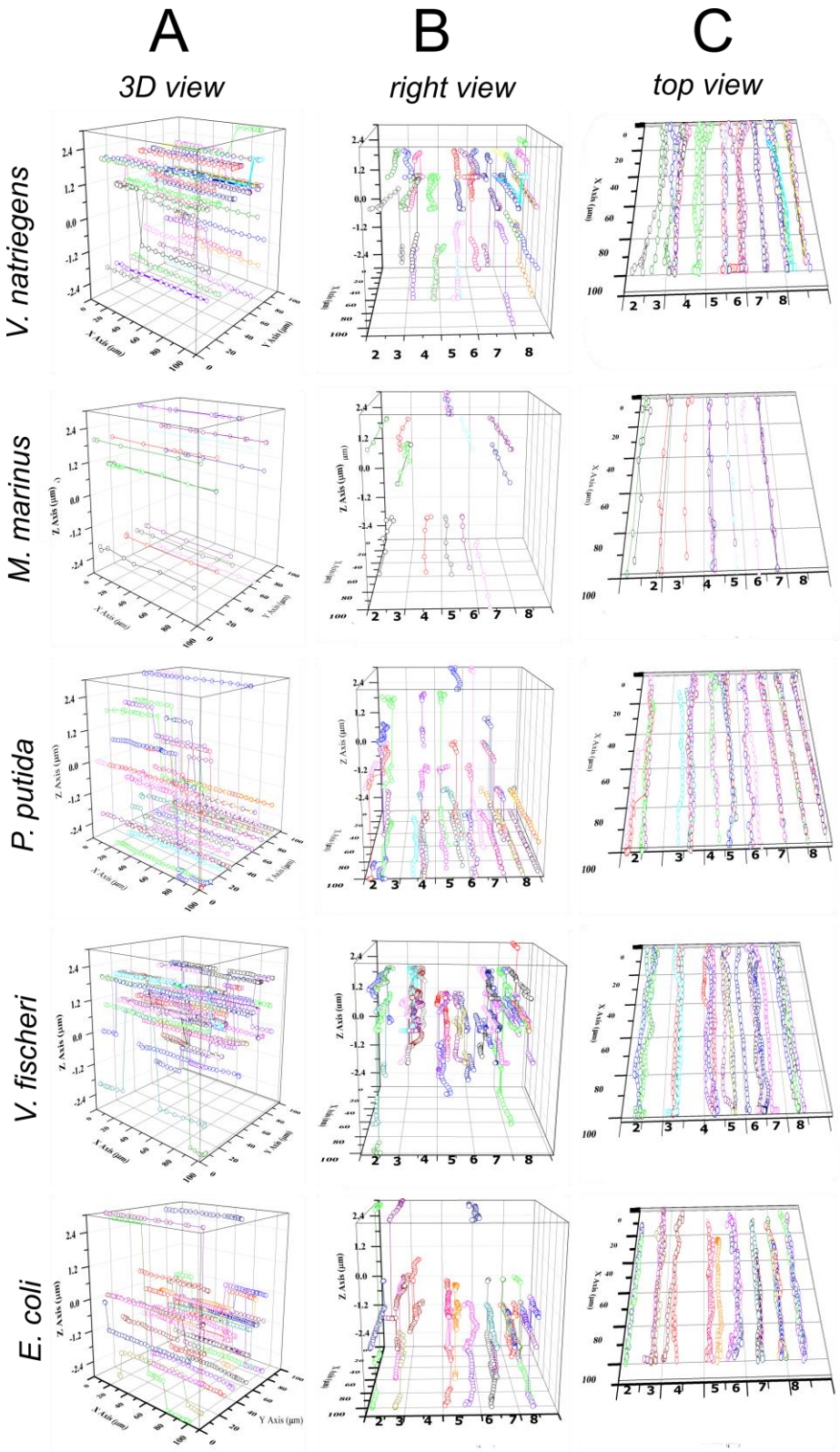

Figure. S10. Cumulative representation of trajectories of five different bacterial species projected in 3D space using z-stack imaging in linear channels.

2.2.1.2. Analysis of the possible sinusoidal motion of bacteria in straight channels

2.2.1.2.1. *Detecting potential helical motion from 2-dimensional camera data with multiple waveforms*

We consider the general problem of determining, from 2D tracking data, whether a bacterium is executing 3D helical motion or 2D, planar "sinusoidal" motion. To do this, we aim to convert 2D data to three dimensions, under the assumption the helical motion is taking place. This then allows us to essentially test the hypothesis of helical motion.

We begin by considering the directional components of the bacterial velocity, derived from positional data. Given a 2D track, we can compute $v_x(t)$ and $v_y(t)$, i.e., the x and y components, as a function of time, while $v_z(t)$, the z-component, is hidden from us due to the use of a point of view placed orthogonally to this axis. Given $v_x(t)$ and $v_y(t)$, our specific goal is to estimate the unobserved velocity component v_z.

Observe that the (unknown) magnitude of the total velocity is given by

$$V(t) = \sqrt{v_x(t)^2 + v_y(t)^2 + v_z(t)^2}$$

At any point where the bacterium is moving orthogonal to the axis of the camera, we have $v_z = 0$, such that the total velocity follows

$$V_\perp = \sqrt{v_x(t)^2 + v_y(t)^2}$$

We now assume (but see below) that the movement of the bacterium has no net drift in the z-direction. This implies the bacterium is moving orthogonal to the camera axis twice in each spiral of its 3D helix.

The total magnitude of velocity can be estimated as a smooth curve fit over the peaks of the $V_\perp$ curve, for instance using spline interpolation. At each peak, $v_z = 0$ and its sign alternates as the helically moving bacterium completes each corkscrew. This allows the estimation of v_z at all other points.

This approach has limitations, because of the loss of information from 3D information being projected into 2D. If the bacterium is moving toward or away from the camera for significant portions of its trajectory, our method is unable to estimate its total v_z component, absent further assumptions about the specific pattern of swimming. In addition, this estimation procedure is inaccurate if the trajectory is not close to a symmetrical, repeatable helix, e.g., if the helical motion is highly stochastic. The technique is inaccurate in the absence of a sufficiently high number of data points, allowing a smooth spline to fit to be applied to the $V_\perp = \sqrt{v_x(t)^2 + v_y(t)^2}$ curve. Lastly, it is not possible, by this approach, to determine the "handedness" of the helix. However, we note that for many bacterial species, the handedness is known or can be determined experimentally, because it is genetically controlled.

Perhaps most crucially, however, this method requires the available tracking data from the camera to contain multiple peaks and troughs of the trajectory, otherwise the spline fitting to the peaks of the $V_\perp$ curve is not possible. For situations where only one or less peak-to-trough sections are available, a different approach is needed.

2.2.1.2.2. Detecting potential helical bacterial motion from 2D camera data where only fragments of sinusoidal tracks are present

In this situation, it is possible to estimate the wavelength of the sinusoidal motion from fragments containing one or two peak-to-trough sections by employing a Fast Fourier Transform (FFT) analysis. Specifically, the FFT spectrum of the *x-y* curve (in 2D) will exhibit one dominant frequency if sinusoidal (potentially resulting from helical motion projected two-dimensionally) is present; otherwise, the spectrum will be highly noisy and/or flat.

We ran all tracks in different channel widths for all five bacterial species through an FFT analysis, leading to the ability to directly fit sine curves to the *x-y* trajectories and estimate the wavelength of the motion in the channel. This approach is illustrated (using a randomly chosen bacterial track from the data set) in Figure X.1 below, in which the right hand side panel shows the results of the fitting procedure and the left hand panel shows the FFT spectrum, exhibiting a dominant frequency. From this, the motion wavelength can be estimated as the inverse of the dominant frequency (code available on request).

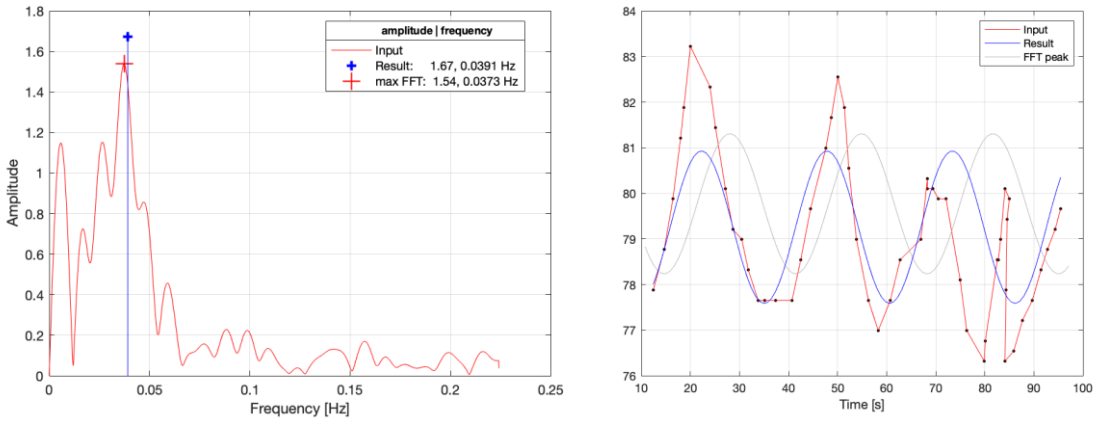

Figure S11. Left: FFT analysis of a bacterial track in a channel, allowing the identification of the frequency of the sinusoidal motion (and thereby the wavelength) as the peak of the FFT spectrum (blue line and red cross). Right: in red, the bacterial track projected as an x-y trajectory; in blue and gray, the resulting sine curve fits corresponding to the FFT peak frequency (gray) and average weighted frequency (blue).

2.2.1.2.3. Estimation of sinusoidal characteristics of bacterial motility in straight channels

We used this method to study the variation in sinusoidal movement (resulting from 3D helical movement) of different bacterial species in different channel widths from 2µm to 8µm. The results are shown in **Figure S12C**.

The sinusoidal character of the motion of *P. putida* and *V. natriegens* varies strongly with the widths of the linear channels, possibly due their shortest body lengths of all species studied. The increase of the wavelength of motion with the increase of the channel widths is probably due to the larger volume available for 3D helical movement. It is notable that a sinusoidal movement has been predicted(22) for monotrichous bacteria (such as *V. natriegens*) and for wall escapers (as partially exhibited by *P. putida*, **Figure 3**).

At the other end of the spectrum, *M. marinus*, with its frequent collisions with and bouncing from the walls, appeared to be insensitive to channel widths with regard to a sinusoidal character of movement.

Finally, in a medium class, *V. fischeri* and especially *E. coli* appear to have only a modest evolution of the sinusoidal character of movement with the increase of the channel widths, possibly due to their longest body lengths in all species studied.

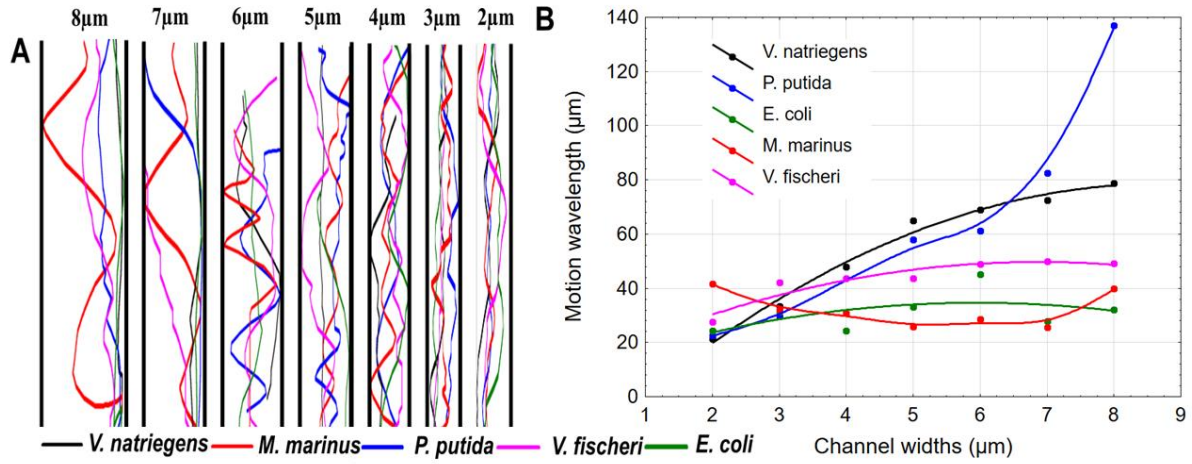

Figure S12. Representative trajectories in the linear channels (A, left); and the variation of the estimated motion wavelengths versus channel widths (B, right).

2.2.1.3. *Velocity in straight channels*

To assess the impact of confinement on bacterial velocity, the average velocity of bacteria was measured, in straight channels, and in plazas, the latter seen as straight channels with 100 µm widths (**Figure S13**).

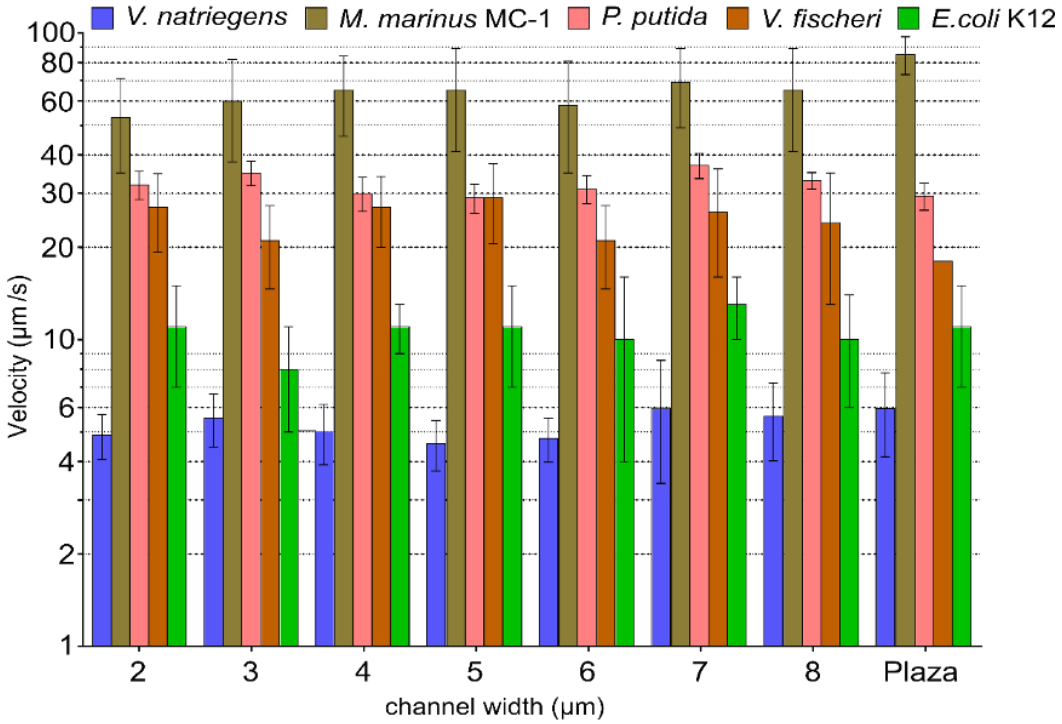

Figure S13. Bacterial velocities (logarithmic scale) in straight channels and plazas.

A moderate decrease was observed for the velocity of *M. marinus*, assumed to be a result of the amplification of the collisions with the walls, but for all other species the velocity does not vary importantly with the channel width.

This observation is further substantiated by the more precise and more detailed measurements of velocities offered by double histograms of velocities in channels (**Figure S14**). Also, with the exception of *M. marinus*, for which extreme narrow channel 'force' motility at the walls, and *V. natriegens* and *E coli*, presenting a bimodal distribution of velocities, towards the channel center, and again a secondary bimodal distribution at the walls (as presented above), all other species behave as swimming parallel to the walls, that is, near the center of the channels, as predicted by **Figure 3**.

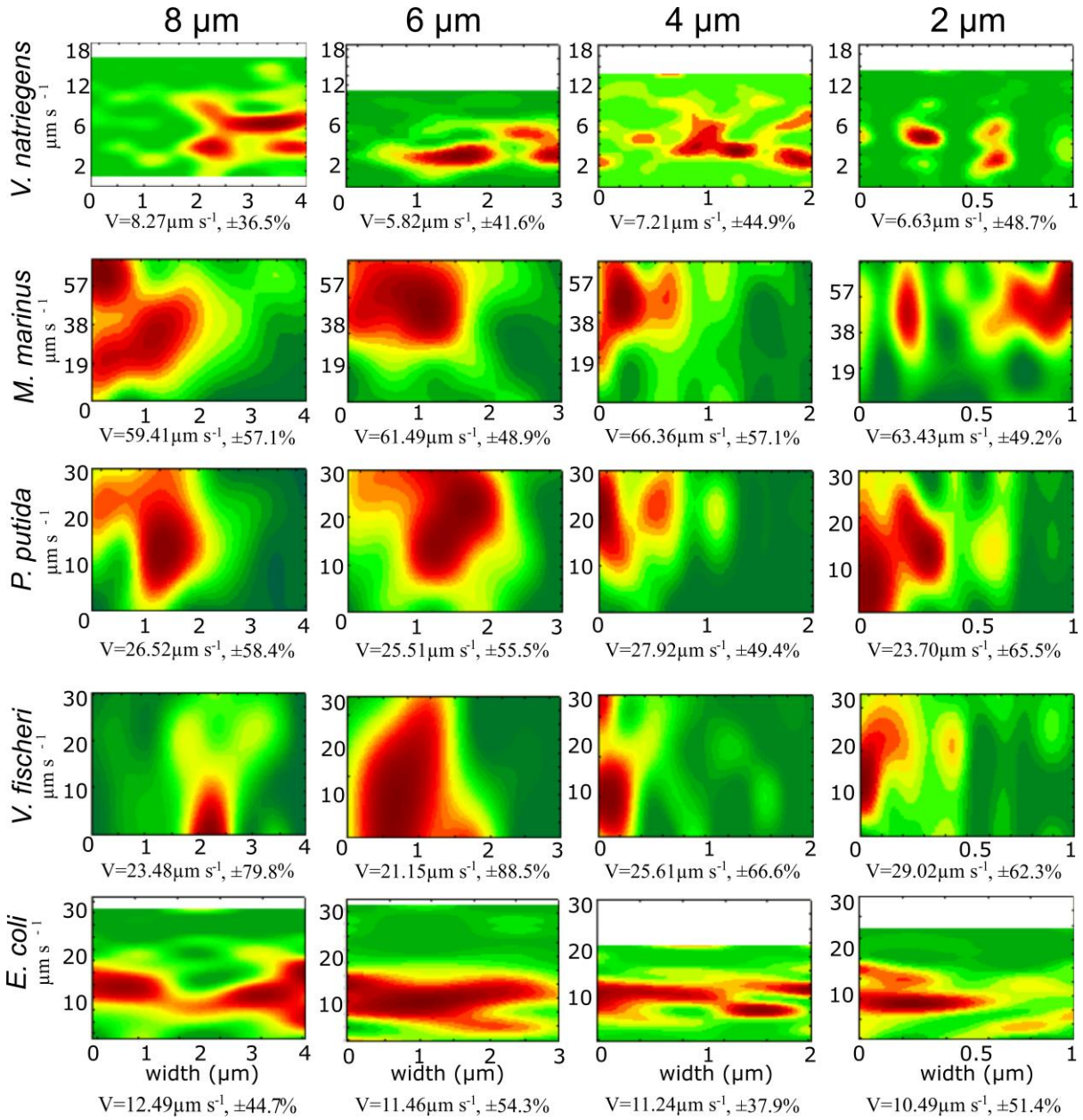

Figure S14. Double histograms of bacterial velocities in linear channels with 2 µm, 4 µm, 6 µm, and 8 µm widths. All velocities values are normalized, i.e., top y-axis value is the maximum. The channel widths are also normalized, i.e., left value on the x-axis represents the channel center, and the right value represents the wall. Note the resilient bimodal distribution, at the walls, for both *V. natriegens* and *E. coli*.

2.3. Motility in channels with angled exits

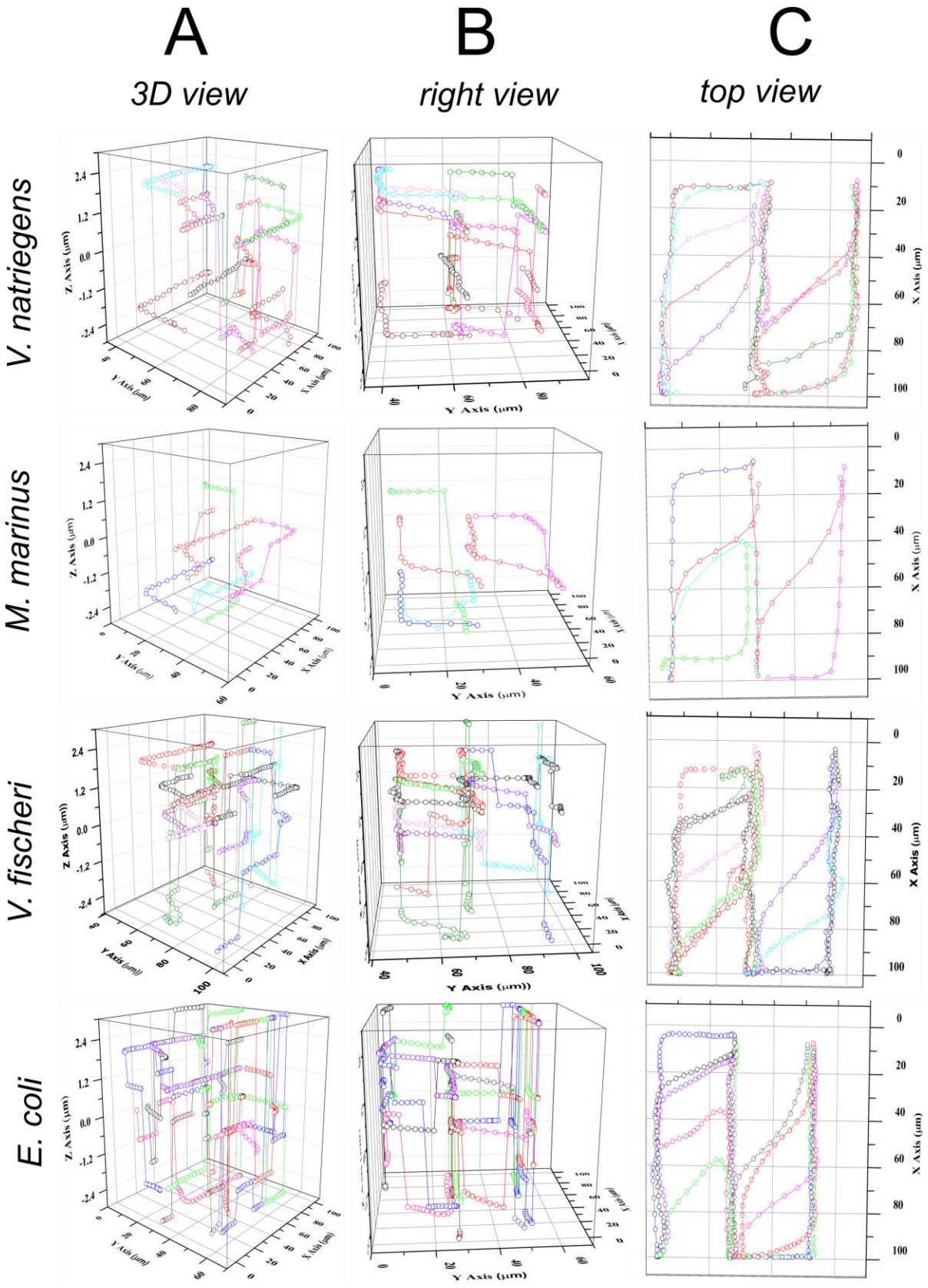

Figure. S15. 3D trajectories of five different bacterial species projected in 3D space using z-stack imaging in angled channels.

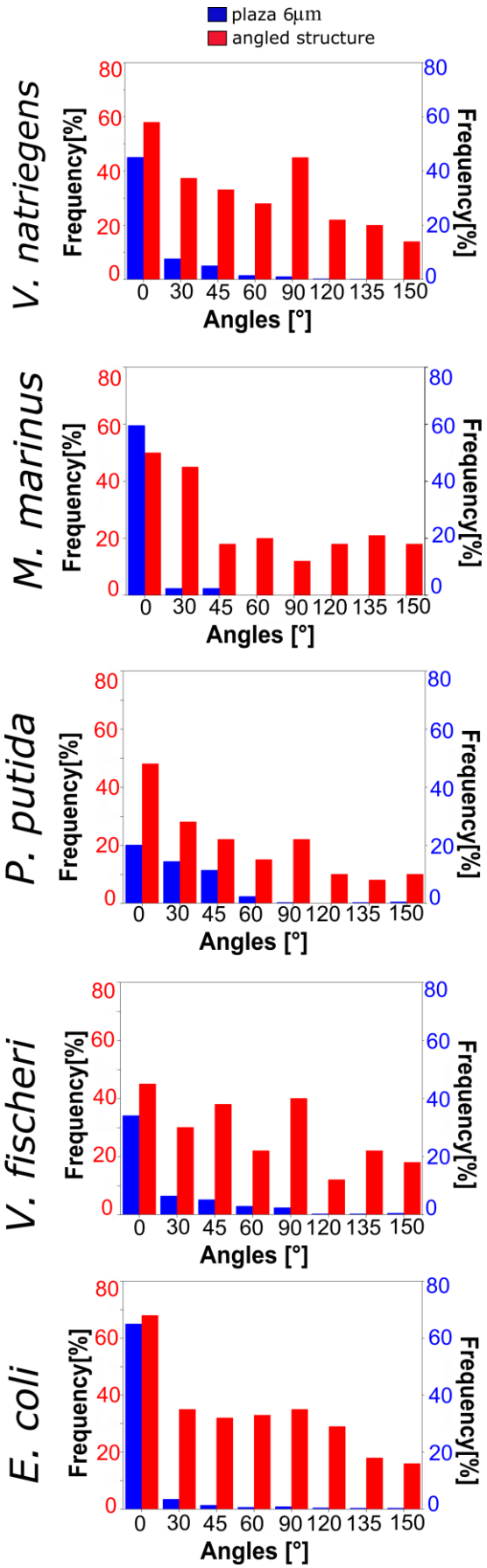

Figure. S16. 3D trajectories of five different bacterial species projected in 3D space using z-stack imaging in angled channels.

2.3.1. Motility in meandered channels

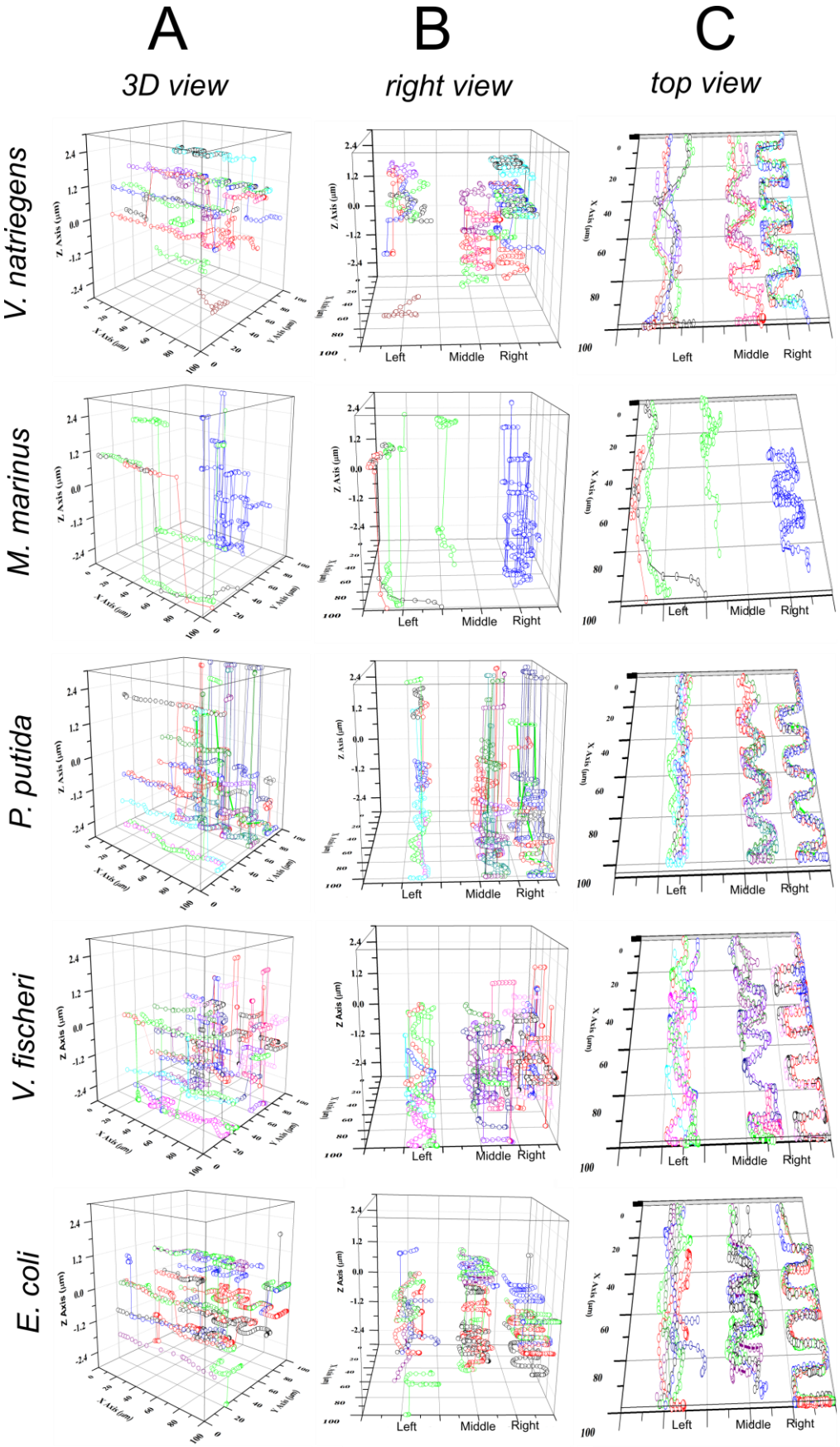

Figure. S17. 3D trajectories of five different bacterial species in meandered channels.

Table S3. Comparison of the average time-spent (seconds) by bacteria in meandered channels with different tooth widths (left-middle-right channels as in **Figure S2C**).

Meandered channels: **Bacteria↓ Tooth length→**	**Left** 5 µm	**Middle** 10 µm	**Right** 15 µm
V. natriegens	4.5 ±1.8	24.0 ±10.2	27.5 ±7.3
M. marinus	3.2 ±2.0	5.5 ±3.3	7.3 ±3.2
P. putida	7.9 ±5.1	11.2 ±4.4	15.4 ±5.6
V. fischeri	9.9 ±5.8	49.1 ±8.9	38.8 ±16.3
E. coli	24.3 ±19.3	43.1 ±14.9	65.9 ±22.3

Table S4: Comparison of the average time-spent (seconds) by bacteria that succeeded in traversing the meandered channels with different tooth widths (left-middle-right channels as in **Figure S2C**).

Meandered channels **Bacteria↓ Tooth length→**	**Average time spent in succeeding the trapping (seconds)**		
	Left 5 µm	**Middle** 10 µm	**Right** 15 µm
V. natriegens	5 ±1.8	NA	28 ±7.4
M. marinus	3 ±2.0	5 ±3.3	7.5 ±3
P. putida	7.5 ±5	11.8±4.4	15.4 ±5.6
V. fischeri	10 ±5.6	38.1 ±8	38.8 ±16.3
E. coli	20.5±18	NA	30 ±22.3

Note that bacterial species like *V. natriegens* and *E. coli* has a zero or negligible success rate in traversing the middle-sized meandered channel during experimental observation.

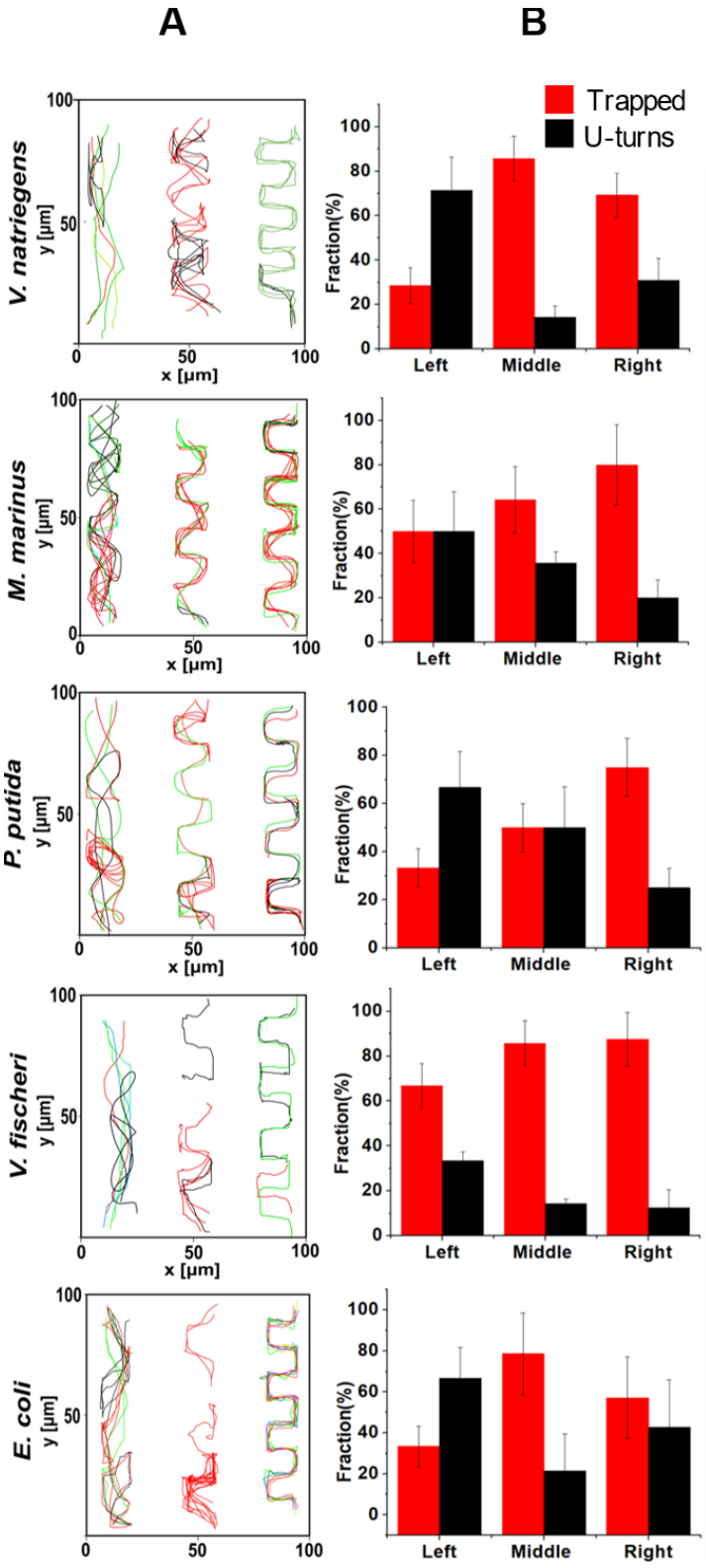

8

Figure S18. Bacterial motility in meandered, comb-like channels. **A**. Representative tracks of the bacterial motility: red trajectories - bacteria took U-turns; black trajectories - bacteria got trapped; any other color - bacteria successfully traversed. **B**. Distribution of unsuccessful bacteria that made either a U-turn or are trapped. By rows, from top to bottom: *V. natriegens* (average count of bacteria each frame, n = 18/frame); *M. marinus* (n = 12/frame); *P. putida* (n = 22/frame); *V. fischeri* (n = 25/frame); and *E. coli* (n = 19/frame).

2.3.4. Velocity distribution for bacterial species in different motility structures –

The velocity observed in various microfluidics structures were expected to be related to the respective levels of confinement, with the highest confinement levels present in the meandered channels ("combs" in **Figure S17**); and the lowest in plazas. However, while the variation of velocity due to confinement were obvious for *M. marinus*, it is far less obvious for other species. However, among the different structures studied here, the motility in the meandered channels present the most noticeable decrease of apparent velocity (with the notable exception of *V. natriegens*). For instance, *E. coli* and *V. fischeri* decreased their velocities by more than 75% compared to its velocity in plazas, and P. putida with almost 50%, This behavior is easily understood if connected with the frequent trapping in the corners of the meandered channels, reducing its overall average velocity. Such steep changes were not observed in the other species, suggesting there was not a strong corner preference for rest of the members of bacteria tested. The velocity differences observed with *E. coli* and *M. marinus* are classical examples of steric interactions-based confinement where *M. marinus* was restricted with space leading to reduction in velocity while for *E. coli* it was the geometrical preferences. Finally, it should be noticed that *V. natriegens* is the species with the smallest aspect ratio of the dimension of cell body, and one the species with the lowest ratio of length/cell diameter (**Figure 3**) which suggest an easier negotiation of convoluted geometries.

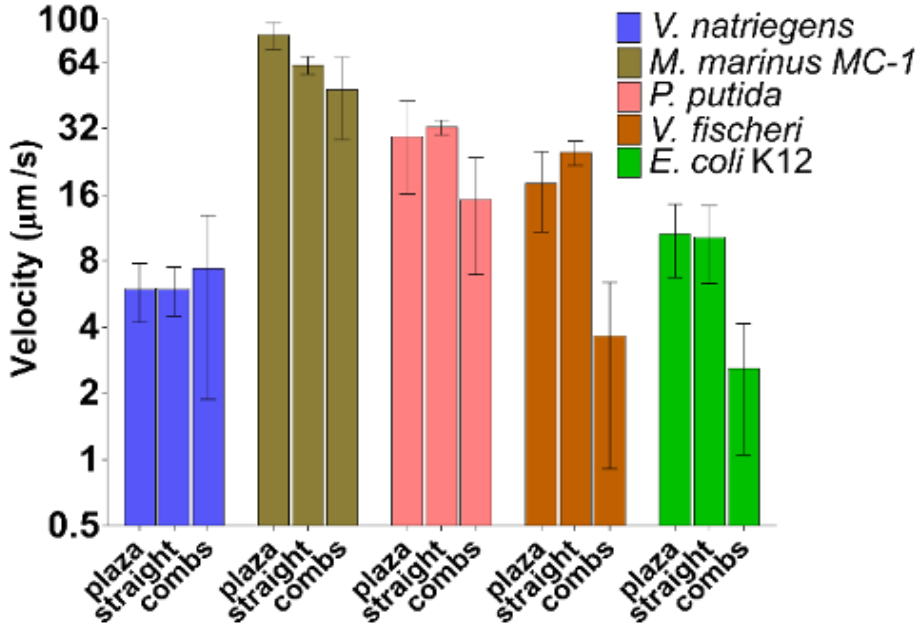

Figure S19. Comparison of bacterial velocities (logarithmic scale) in plazas, straight channels ("straight" label) and meandered channels ("combs" label).

2.8. Tight geometrical like confinements from nature

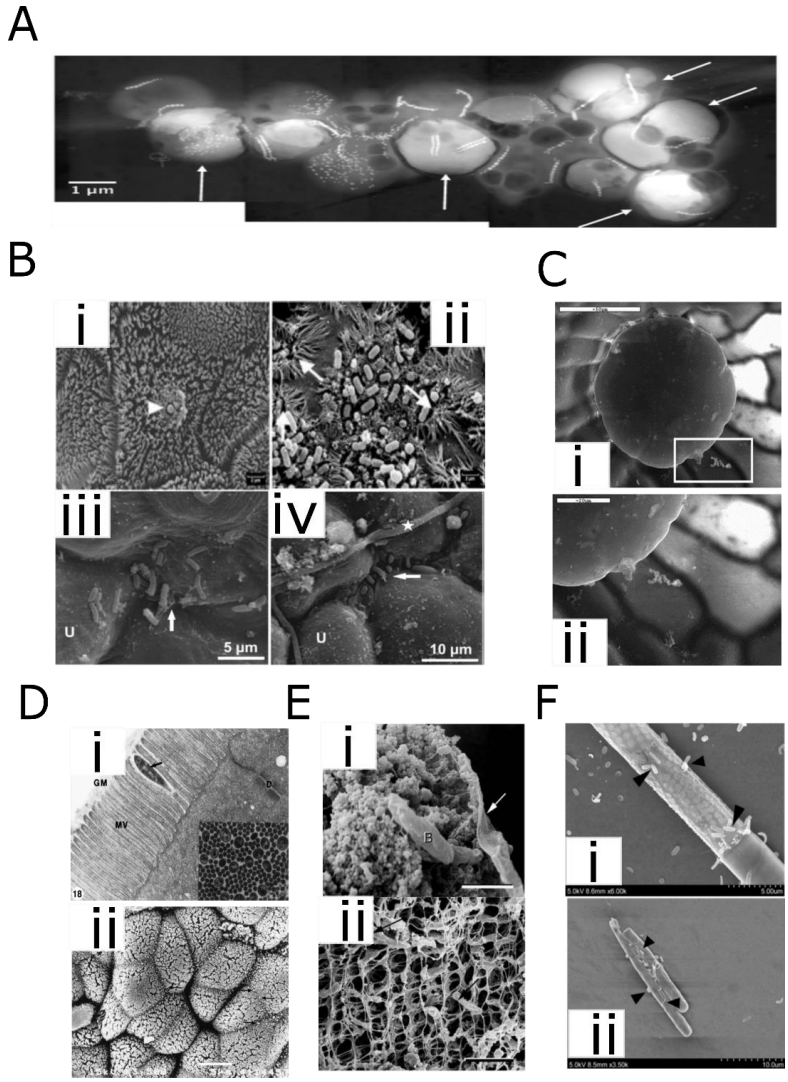

Figure S20. Closer look into the microbial habitats and tight confinements in nature. The above images are adopted from several reported communications, which shows high definition microenvironment that are bacterial habitats and the tight confinements that are common observations among these figures. **A.** *Magnetotactic species* in the soil sediments of lake (23, 24), spherical bacteria in the constrained environments. **B**. *Escherichia species* in the gut (B I & ii) and on plant surfaces (25) (B iii & iv) . The image shows constricted patterns with tight channel like features and different turn angles (iii & iv). **C**. Rod shaped bacterial species (26) . The image shows several straight and different turn angles, like the feature that we used in the devices for studying angled preferences. **D**. *Vibrio species* in the gut of fishes (27). The image D(i) shows straight channel like feature present in the microvilli (MV) and image D(ii) shows different angled and zig-zag patterns, like the structures with higher complexity that we explored in our studies. **E**. *Pseudomonas species* in soil sediments (i &ii) shows features with different pore sizes and highly complex structures (28). **F**. rod shaped bacterium on surface of phytoplankton (29). The figure shows straight lines with many turn angles and most notably 90° turn angles.

Supporting Movies

The movies present typical motility patterns of all bacterial species studied. *E. coli* and *V. natriegens* were labelled with fluorescent expressing plasmids (either GFP or mCherry) and the movies were recorded with a fluorescence microscope. Other species were observed in bright field (all species) or in dark field (*M. marinus* only). All the movies are played at original speed to show different behaviors like the velocity differences among the different species, U-turn types, wall-accumulating and wall repelling motions, circular, chaotic trajectories etc.

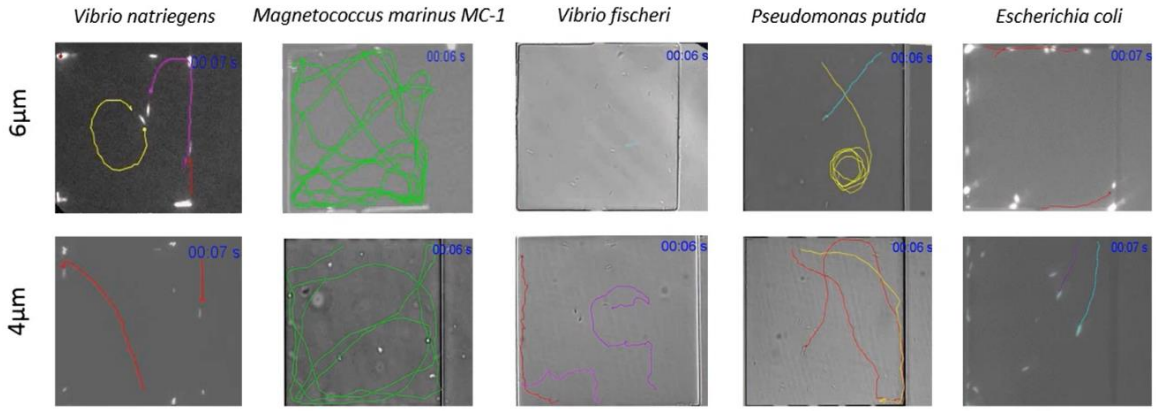

Supporting Movie 1 – Bacterial motility in quasi open spaces (plazas) of two different heights

Trajectories along the walls: Red, Ping-Pong like trajectories: Green, Circular trajectories (longest): Purple, Circular trajectories (Smallest): Yellow, Random trajectories: Cyan

Movie S1. Motility in quasi-open spaces (plazas). Bacterial specific motility observed from the movies and discussed in the main text – Screen shots of the videos is presented here, while the actual movies can be downloaded.
V. natriegens: Preference towards the corners and wall-directed motility. *M. marinus:* Wall-bouncing, ping-pong ball like motility pattern. Restricted motility and few straight trajectories in 4 µm tall plazas, as an effect of confinement. *V. fischeri:* Wiggling, chaotic motion with frequent pauses and change of directions. Observable frequently in 4 µm low plazas. *P. putida:* Typical circular motions with high deflection angles. The diameter of the circular motion decreases due to vertical confinement in 4 µm low plazas. *E. coli:* Wall-dependent motility with corner preferences. Also, small circular motions observed in both high and low plazas.

Linear channels

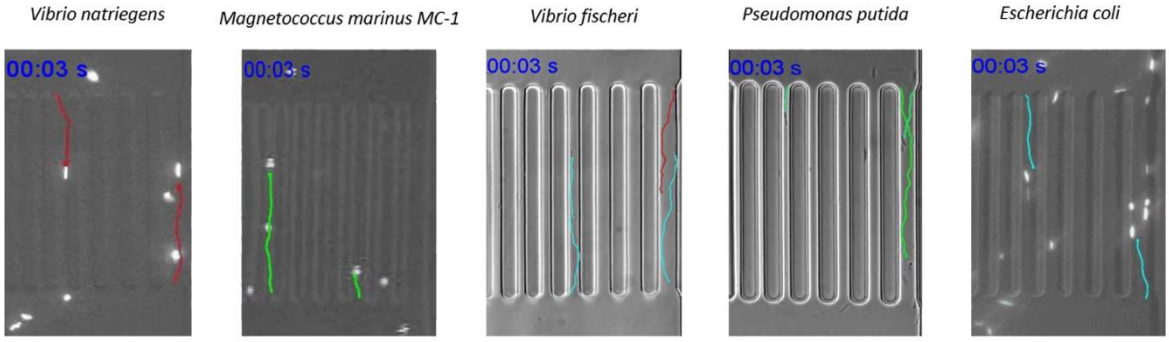

Supporting Movie 2 – Bacterial motility in linear channels

Trajectories along the walls: Red, Sinusoidal like trajectories: Green, Random trajectories: Cyan

Movie S2. Bacterial motility in linear channels. *V. natriegens:* Lowest U-turn frequency with high accumulating. *M. marinus:* High U-turn frequency in narrow channels due to repeated sinusoidal (bouncing) motility and deflection from the walls. *V. fischeri:* Chaotic motility pattern with considerable U-turn frequency, irrespective of the channel dimensions. *P. putida:* Sinusoidal (bouncing) motility and deflection from the walls. *E. coli:* Second highest propensity for wall-accumulating and a low U-turn frequency.

Angled channels

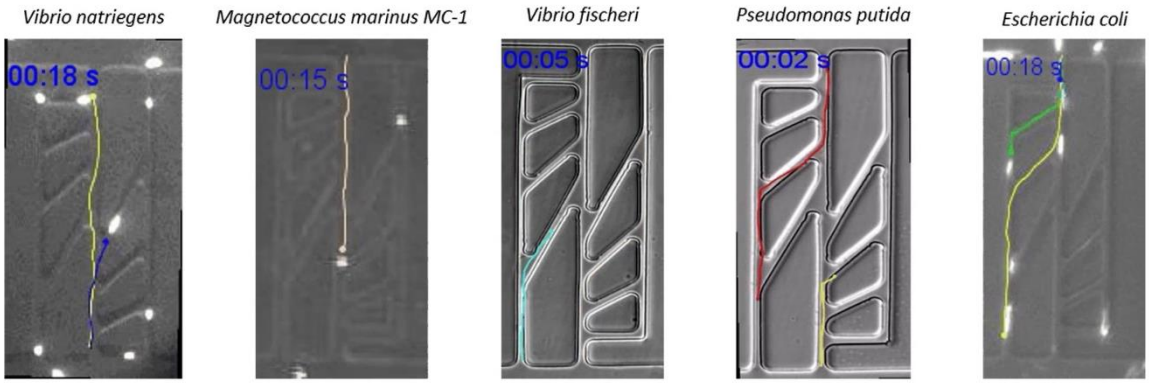

Supporting Movie 3 – Bacterial motility in angled channels

Movie S3. Bacterial motility in angled channels. *V. natriegens:* Preference for moving on straight trajectories along the middle axis channel. *M. marinus:* Trajectories deflected at angles > 135°. *V. fischeri:* Higher U-turn % and partly wall-accumulating behavior at angled channels. *P. putida:* Trajectories deflected at angles > 135°. *E. coli*: Preference for moving on straight trajectories along the middle axis channel.

Combed channels

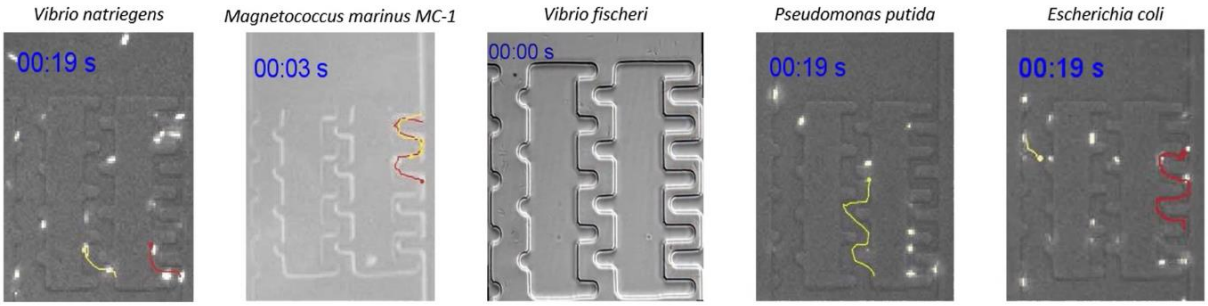

Supporting Movie 4 – Bacterial motility in combed structures

Successful trajectories: Red, Unsuccessful trajectories: Yellow

Movie S4 - Bacterial motility in combed structures. *V. natriegens:* Successfully traversed the combs of lowest and highest tooth length, but not the middle combed-structures due to trapping at the corners. *M. marinus*: Successfully traversed the middle tooth structures compared to the other two combed structures. Least success rate in combs. *V. fischeri:* Possessed a corner–to-corner motility pattern, providing a higher success rates in traversing in all the three comb types. *P. putida:* Exhibited a shifted propensity to follow walls for traversing the combs. Still a second lowest success rate in navigating the complicated comb structures. *E. coli:* 90°: angled corners appear to operate as traps, for *E. coli* very efficiently in middle sized tooth, while the two other combs were successfully traversed.

References for Supporting Information Section

1. S. Cheng *et al.*, Microscopical observation of the marine bacterium Vibrio natriegeus growth on metallic corrosion. *J Materials, Manufacturing Processes* **25**, 293-297 (2010).
2. M. T. Weinstock, E. D. Hesek, C. M. Wilson, D. G. Gibson, Vibrio natriegens as a fast-growing host for molecular biology. *Nature Methods* **13**, 849 (2016).
3. D. A. Bazylinski *et al.*, Magnetococcus marinus gen. nov., sp. nov., a marine, magnetotactic bacterium that represents a novel lineage (Magnetococcaceae fam. nov., Magnetococcales ord. nov.) at the base of the Alphaproteobacteria. *Int J Syst Evol Microbiol* **63**, 801-808 (2013).
4. S. Taherkhani, M. Mohammadi, J. Daoud, S. Martel, M. Tabrizian, Covalent binding of nanoliposomes to the surface of magnetotactic bacteria for the synthesis of self-propelled therapeutic agents. *ACS Nano* **8**, 5049-5060 (2014).
5. M. L. Davis, L. C. Mounteer, L. K. Stevens, C. D. Miller, A. Zhou, 2D motility tracking of Pseudomonas putida KT2440 in growth phases using video microscopy. *J Biosci Bioeng* **111**, 605-611 (2011).
6. J. W. Barton, R. M. Ford, Determination of effective transport coefficients for bacterial migration in sand columns. *Appl Environ Microbiol* **61**, 3329-3335 (1995).
7. M. S. Hendrie, W. Hodgkiss, J. M. Shewan, Proposal that Vibrio marinus (Russell 1891) Ford 1927 be Amalgamated with Vibrio fischeri (Beijerinck 1889) Lehmann and Neumann 1896. *International Journal of Systematic and Evolutionary Microbiology* **21**, 217-221 (1971).
8. D. S. Millikan, E. G. Ruby, Alterations in Vibrio fischeri motility correlate with a delay in symbiosis initiation and are associated with additional symbiotic colonization defects. *Appl Environ Microbiol* **68**, 2519-2528 (2002).
9. M. Binz, A. P. Lee, C. Edwards, D. V. Nicolau, Motility of bacteria in microfluidic structures. *Microelectronic Engineering* **87**, 810-813 (2010).
10. H. C. Berg, *E. coli in Motion* (Springer Science & Business Media, 2008).
11. F. Alejandro Bonilla, N. Kleinfelter, J. H. Cushman, Microfluidic aspects of adhesive microbial dynamics: A numerical exploration of flow-cell geometry, Brownian dynamics, and sticky boundaries. *Advances in Water Resources* **30**, 1680-1695 (2007).
12. J. M. Swiecicki, O. Sliusarenko, D. B. Weibel, From swimming to swarming: Escherichia coli cell motility in two-dimensions. *Integr Biol (Camb)* **5**, 1490-1494 (2013).
13. C. Acikgoz, M. A. Hempenius, J. Huskens, G. J. Vancso, Polymers in conventional and alternative lithography for the fabrication of nanostructures. *European Polymer Journal* **47**, 2033-2052 (2011).
14. D. Qin, Y. Xia, G. M. Whitesides, Soft lithography for micro- and nanoscale patterning. *Nat Protoc* **5**, 491-502 (2010).
15. M. Gan, J. Su, J. Wang, H. Wu, L. Chen, A scalable microfluidic chip for bacterial suspension culture. *Lab on a Chip* **11**, 4087-4092 (2011).
16. R. Watteaux, R. Stocker, J. R. Taylor, Sensitivity of the rate of nutrient uptake by chemotactic bacteria to physical and biological parameters in a turbulent environment. *J Theor Biol* **387**, 120-135 (2015).
17. C. A. Schneider, W. S. Rasband, K. W. Eliceiri, NIH Image to ImageJ: 25 years of image analysis. *Nat Methods* **9**, 671-675 (2012).
18. E. Meijering, O. Dzyubachyk, I. Smal, Methods for cell and particle tracking. *Methods Enzymol* **504**, 183-200 (2012).

19. K. Bente *et al.*, High-speed motility originates from cooperatively pushing and pulling flagella bundles in bilophotrichous bacteria. *eLife* **9** (2020).
20. H. Shum, E. A. Gaffney, D. J. Smith, Modelling bacterial behaviour close to a no-slip plane boundary: The influence of bacterial geometry. *Proceedings of the Royal Society A: Mathematical, Physical and Engineering Sciences* **466**, 1725-1748 (2010).
21. S. E. Spagnolie, E. Lauga, Hydrodynamics of self-propulsion near a boundary: predictions and accuracy of far-field approximations. *Journal of Fluid Mechanics* **700**, 105-147 (2012).
22. H. Shum, E. A. Gaffney, Hydrodynamic analysis of flagellated bacteria swimming in corners of rectangular channels. *Physical Review E - Statistical, Nonlinear, and Soft Matter Physics* **92** (2015).
23. S. Rivas-Lamelo *et al.*, Magnetotactic bacteria as a new model for P sequestration in the ferruginous Lake Pavin. (2017).
24. P. Dean, M. Maresca, S. Schüller, A. D. Phillips, B. J. P. o. t. N. A. o. S. Kenny, Potent diarrheagenic mechanism mediated by the cooperative action of three enteropathogenic Escherichia coli-injected effector proteins. **103**, 1876-1881 (2006).
25. K. Karamanoli *et al.*, Are leaf glandular trichomes of oregano hospitable habitats for bacterial growth? **38**, 476-485 (2012).
26. L. E. B. Baldotto, F. L. J. C. j. o. m. Olivares, Phylloepiphytic interaction between bacteria and different plant species in a tropical agricultural system. **54**, 918-931 (2008).
27. E. Ringø, R. E. Olsen, T. M. Mayhew, R. J. A. Myklebust, Electron microscopy of the intestinal microflora of fish. **227**, 395-415 (2003).
28. M. M. Baum *et al.*, Characterization of structures in biofilms formed by a Pseudomonas fluorescens isolated from soil. **9**, 103 (2009).
29. I. L. Bagatini *et al.*, Host-specificity and dynamics in bacterial communities associated with bloom-forming freshwater phytoplankton. **9**, e85950 (2014).